Nuclear Engineering and Technology 57 (2025) 103686

Contents lists available at ScienceDirect

Nuclear Engineering and Technology

journal homepage: www.elsevier.com/locate/net

Original Article

In-depth understanding of sodium heat transfer characteristics with low Prandtl number in wire-wrapped fuel assemblies using high-fidelity CFD technique

Jophous Mugabi [a], Hanseop Song [a], Jae-Ho Jeong [a,*]

[a] School of Mechanical Engineering, Chung-Ang University, 84, Heukseok-ro, Dongjak-gu, Seoul, 06974, the Republic of Korea

ARTICLE INFO

Keywords:
Sodium-cooled fast reactor (SFR)
Wire-wrapped fuel bundle
Low Prandtl number fluids
Computational Fluid Dynamics (CFD)
Thermal-hydraulic analysis
Heat transfer optimization
STAR-CCM+ and ANSYS CFX

ABSTRACT

Understanding the thermal-hydraulic behavior of sodium-cooled fast reactors is crucial for optimizing their performance and safety. This study investigates the unique low Prandtl number properties of liquid sodium coolant, which influence heat transfer and fluid dynamics in turbulent flows within wire-wrapped fuel bundles. Using a combination of experimental data and high-fidelity Computational Fluid Dynamics (CFD) simulations, we analyzed key thermal-hydraulic characteristics for the ORNL 19-pin, Toshiba 37-pin, WARD 61-pin, and KAERI 61-pin fuel bundles under various heating and flow conditions. CFD simulations were conducted in STAR-CCM+ and ANSYS CFX and examined mass flow rates, pressure drops, and temperature distributions, validated against experimental data. Sensitivity analyses of turbulence models (SST, k-ε, and k-ω) indicated that the SST model best captured complex flow and three-dimensional vortical structures in SFR conditions, with edge subchannels exhibiting enhanced heat transfer due to higher axial velocities. Code-to-code comparisons confirmed strong agreement in predicted results, with STAR-CCM + aligning more closely with experimental data in some cases. The study underscores the importance of advanced CFD techniques in accurately modeling thermal management in wire-wrapped fuel bundles, contributing to improved safety and efficiency in SFR systems.

1. Introduction

The Generation IV Sodium-Cooled Fast Reactor (SFR) leverages fast neutrons for fission reactions and uses liquid sodium as a coolant to effectively manage heat transfer. Research into the thermal-hydraulic characteristics of SFRs is crucial in nuclear engineering to understand how liquid sodium behaves as a coolant, focusing specifically on its heat transfer and fluid flow properties. Effective coolant circulation and heat transfer are essential to prevent overheating, which could otherwise lead to equipment failures and safety risks. Researchers utilize both experimental and computational approaches to explore the thermal-hydraulic performance of SFRs. Experimental studies test reactor components under various operating conditions to observe their real-world behavior, while computational studies use mathematical models and simulations to predict how the coolant and reactor components perform under different conditions. Of particular interest are the thermal-hydraulic characteristics of fuel bundles, which are commonly analyzed through Subchannel analysis codes and CFD methods.

Subchannel analysis codes divide the reactor core into smaller sections, or subchannels, to study the flow and heat transfer processes within each segment. This method enables accurate predictions of the coolant's behavior throughout the reactor core. For example, Kim et al. (2002) validated the MATRA-LMR Subchannel code by varying flow areas within subchannels to model flow fields affected by wire spacers [1]. Memmott et al. (2010) developed a RELAP5-based model to assess Subchannel performance in advanced fuel designs, such as annular fuel rod arrangements [2]. Similarly, Sun et al. (2018) used the SUVAC Subchannel code to benchmark experiments involving the ORNL 19-pin, Toshiba 37-pin, and EBR-II SHRT-17 tests [3]. On the other hand, CFD codes allow for detailed modeling of complex flow patterns and heat transfer, such as turbulence, convective heat transfer, and coolant mixing in SFRs. For instance, Fricano et al. (2014) conducted a CFD benchmark study on the ORNL 19-pin sodium test assembly, performing sensitivity analyses on mesh size, turbulence, and wire contact models [4]. Additionally, Jeong et al. (2021) analyzed a JAEA 7-pin fuel bundle experiment using CFD and found that adjusting the turbulent Prandtl number to 0.02 based on heat transfer correlations improved predictive accuracy for complex heat transfer processes [5].

* Corresponding author.
E-mail addresses: mugajoph@cau.ac.kr (J. Mugabi), seap1998@gachon.ac.kr (H. Song), jaehojeong@cau.ac.kr (J.-H. Jeong).

https://doi.org/10.1016/j.net.2025.103686
Received 15 November 2024; Received in revised form 27 January 2025; Accepted 3 May 2025
Available online 8 May 2025

The Prandtl number is a dimensionless factor that compares momentum diffusivity to thermal diffusivity in a fluid. Sodium, with its low Prandtl number, is particularly suitable for SFRs due to its high thermal conductivity, low vapor pressure, and high boiling point, which allow it to transfer heat efficiently at elevated temperatures without boiling. This unique property enables effective heat transfer while minimizing momentum transfer, which is ideal for the wire-wrapped fuel bundles used in SFRs. Despite these advantages, using sodium as a coolant presents specific challenges. Sodium's reactivity with air and water necessitates stringent safety and maintenance protocols, and its low heat capacity can lead to rapid temperature changes, potentially causing thermal stress in reactor components. Nevertheless, sodium remains a promising coolant option, and ongoing research aims to address its challenges while maximizing its heat transfer potential. Studies on the heat transfer properties of sodium with a low Prandtl number have been extensive, focusing on factors such as heat transfer coefficients, flow characteristics, and pressure drops in high-temperature environments. For example, He et al. (2022) examined the heat transfer characteristics of sodium in a wire-wrapped fuel pin bundle, finding that the heat transfer coefficient increases with Reynolds number and that the wire-wrapped structure improves heat transfer efficiency [6]. Song et al. (2019) assessed various turbulence models for sodium's heat transfer in wire-wrapped bundles, concluding that the k-ω SST turbulence model provided the most accurate predictions [7]. These studies emphasize the significance of understanding the heat transfer characteristics of sodium with a low Prandtl number in SFRs. By optimizing the design and operation of sodium cooling systems, it is possible to improve the efficiency and safety of SFRs, making them a sustainable and reliable energy source.

In this study, we aim to further examine the heat transfer characteristics of low Prandtl number fluids, with an emphasis on sodium, through a CFD benchmark study comparing experimental results with CFD-derived data. Datasets from established sources such as Oak Ridge National Laboratory (ORNL), Toshiba Institute of Nuclear Engineering, and the Westinghouse Advanced Reactors Division (WARD) were utilized. This study focuses on evaluating the accuracy of CFD models in predicting the heat transfer behaviors of low Prandtl number fluids, including comparisons across varying turbulent Prandtl numbers, explanations of CFD methodology (including governing equations, numerical methods, boundary conditions, and mesh configurations), and the effects of vortex structures on heat transfer. By examining the impact of turbulent Prandtl numbers on heat transfer in low Prandtl number fluids, the researchers aim to enhance the understanding of these heat transfer mechanisms and validate CFD models for such conditions. The findings of this research will provide valuable insights into the behavior of low Prandtl number fluids, contributing to the optimization and safety of sodium-cooled fast reactor designs.

2. Prandtl number

In SFRs, liquid metals like sodium are uniquely suited as coolants due to their low Prandtl number, which reflects a distinctive balance between thermal and momentum diffusivity. This low Prandtl number arises from sodium's high thermal conductivity, low viscosity, and high density, allowing it to transfer heat efficiently in high-temperature environments while maintaining a stable flow. The resulting heat transfer behavior is characterized by a thicker thermal boundary layer compared to the momentum boundary layer, a feature that distinguishes liquid metals from conventional fluids such as air or water. Despite these advantages, predicting and modeling turbulent heat transfer in low Prandtl number fluids presents significant challenges [8]. Standard turbulence models, which are designed for conventional fluids with Prandtl numbers near unity, fail to accurately capture the unique thermal and flow dynamics of liquid metals. For example, the Reynolds analogy, which assumes a similarity between momentum and thermal transport, does not hold for these fluids [9]. In traditional fluids, engineers often use a constant turbulent Prandtl number (Pr_t) of around 0.85–1.0 to simplify heat transfer analysis. However, for liquid metals with Prandtl numbers far below 1, such assumptions are unreliable and lead to inaccuracies in predicting heat transfer behavior.

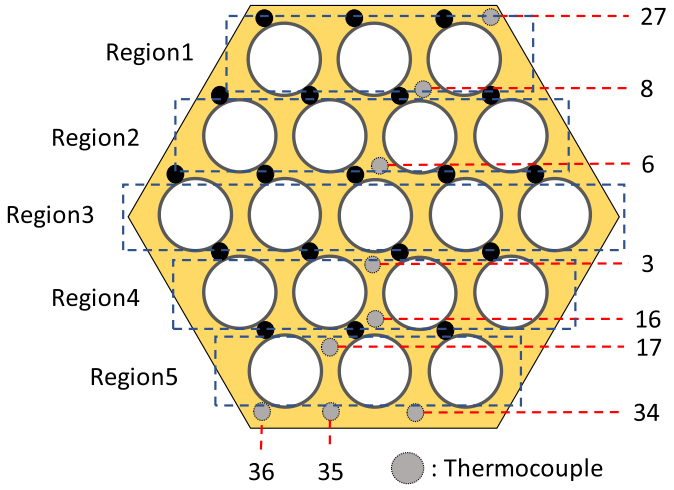

Fig. 1. The ORNL 19-pin fuel bundle schematic shows the location of thermocouples and subchannel numbers (3, 6, 8, 16, 17, 27, 34, 35, and 36) and power skew regions (1–5).

Research has shown that the turbulent Prandtl number for liquid metals deviates significantly from the values used for conventional fluids. Numerical studies demonstrate that low Prandtl number fluids require tailored turbulence models that incorporate variable turbulent Prandtl numbers [10–13]. For instance, in analyzing a 37-pin wire-wrapped fuel bundle at the PLANDTL facility, researchers found that an optimal turbulent Prandtl number of 0.02 closely matched experimental data, significantly improving the accuracy of heat transfer correlations and radial temperature distribution predictions [14]. Commercial CFD codes, which often rely on constant turbulent Prandtl numbers, are inadequate for analyzing liquid metal flows, as they typically calculate turbulent viscosity using approaches like k-ε or k-ω turbulence models while assuming a fixed Pr_t value at the start of calculations. For liquid metals, this oversimplification neglects key factors such as buoyancy effects and the interplay of high thermal conductivity with low viscosity. Addressing these challenges requires the development of advanced turbulence models specifically tailored to the unique properties of liquid metals. Such models must move beyond constant Pr_t assumptions to accurately capture the distinct dynamics of liquid metals, incorporating variable turbulent Prandtl numbers and other relevant factors. These advancements are essential not only for improving the accuracy of heat transfer predictions but also for enhancing the performance, efficiency, and safety of next-generation nuclear reactors, solidifying the role of liquid metals like sodium as exceptional coolants in advanced reactor designs.

3. Methodology and validation of the test section

3.1. Introduction to testing facilities

3.1.1. ORNL 19-pin fuel assembly

The Oak Ridge National Laboratory (ORNL) conducted experiments on a 19-pin wire-wrapped fuel bundle at the Fuel Failure Mockup (FFM) facility, designed for high-temperature sodium testing of Liquid Metal Fast Breeder Reactor (LMFBR) fuel bundles [15]. The benchmark bundle, labeled 2A, consists of 19 simulated fuel rods arranged in a hexagonal duct. This setup uses electric heaters that mimic the power density and geometry of actual LMFBR fuel rods, allowing researchers to study the effects of power distribution across the bundle. Temperature

Table 1
Geometric information of the test sections of the fuel assembly.

Geometry parameters	ORNL 19-pin	Toshiba 37-pin	WARD 61-pin	KEARI 61-pin
Number of pins	19	37	61	61
Pin diameter (mm)	5.84	6.5	13.18	8
Pin pitch (mm)	7.26	7.87	14.26	9.12
Total Pin length (mm)	914.4	1328	1624	238.9
Wire diameter (mm)	7.26	1.32	0.9398	1
Wire lead pitch (mm)	304.8	307	101.5	238.9
Heated length (mm)	533.4	1328	1143	1500
Duct inside the flat-to-flat distance (mm)	64.1	50.4	113.88	150
Pitch-to-diameter (P/D)				1.14
Height-to-diameter (H/D)				29.86
Coolant	Sodium	Sodium	Sodium	Water (60 °C)

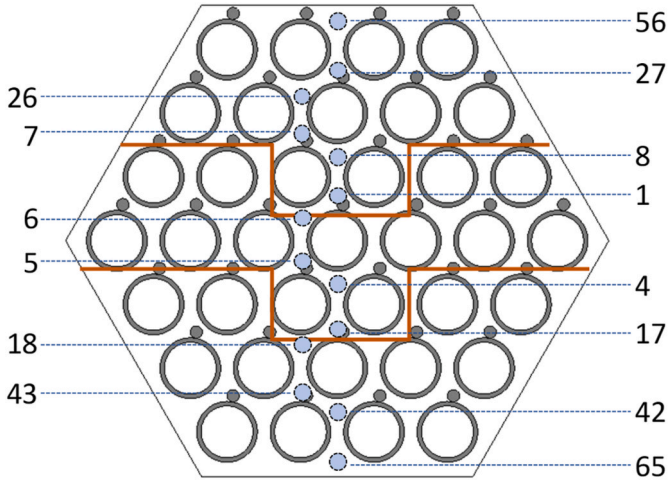

Fig. 2. The Toshiba 37-pin fuel bundle schematic shows the location of thermocouples and subchannel numbers at the top of the heated section and the 3 power skew regions.

measurements are collected by two thermocouples per wire-wrap (providing 38 total measurements) and 11 additional thermocouples at the outlet. The FFM-2A experiment, which was selected as the benchmark case for this study, aims to determine the temperature distribution within the load bundle, at the channel wall, and at the outlet. The fuel rod has a diameter of 5.84 mm and a pitch-to-diameter ratio (P/D) of 1.244. It is positioned at the center of a hexagonal duct, which has an internal flat-to-flat distance of 64.1 mm. The wire spacers have a diameter of 7.26 mm and a lead pitch of 304.8 mm. The heated length of the fuel rod is 533.4 mm, and it is heated under conditions of uniform heat flux distribution. Fig. 1 illustrates a schematic of the ORNL 19-pin fuel bundle showing the radial power (skew) distribution across the bundle. The design specifications for the 19-pin fuel bundle are summarized in Table 1. The facility allows independent control of heater groups, enabling various combinations to operate at power levels of up to 24.5 kW each. This setup enables the study of power distribution effects and power skew across the rod bundle.

3.1.2. Toshiba 37-pin fuel assembly

The Toshiba Institute of Nuclear Engineering conducted tests on a 37-pin wire-wrapped fuel bundle using the Sodium Heat Transfer Test Loop (SHEL) to study heat transfer in LMFBR reactors under natural circulation conditions [16]. This setup is designed to evaluate the effects of buoyancy on heat transfer within the rod bundle and to validate the COBRA-IV-I code at low flow rates characteristic of natural circulation. Although the Toshiba test assembly differs in the number of rods compared to a typical LMFBR bundle, it shares similar thermal and hydraulic properties, enabling reliable comparisons.

In the Toshiba setup, electric heaters are utilized in the simulation of the fuel rods within the reactor. Each rod has a diameter of 6.5 mm and a P/D ratio of 1.21 and it is positioned in a hexagonal duct with a 64.1 mm flat-to-flat distance. Steel wire-wrap spacers of 1.32 mm diameter are arranged with a lead pitch of 304.8 mm, while the heated length of each rod extends to 1328 mm. The rods are heated with a chopped cosine heat flux distribution, with an average-to-maximum ratio of 1.21. Table 1 summarizes the design specifications of the Toshiba 37-pin fuel bundle test section. The test assembly is integrated into the primary sodium loop, transferring heat to a secondary loop through an intermediate heat exchanger. An air blast heat exchanger in the secondary loop serves as the final heat sink. Sodium circulation is managed by electromagnetic pumps, and three power control units independently supply power to designated regions within the bundle, generating a distinct radial power distribution. As illustrated in Fig. 2, this radial power skew within the rod bundle is achieved through the three divided regions.

3.1.3. WARD 61-pin fuel assembly

The Westinghouse Advanced Reactors Division (WARD) developed a 61-pin fuel bundle for experimental analysis of thermal behavior within fuel assemblies [17]. This experiment focuses on the influence of inter-assembly heat transfer on peak temperatures and the effect of buoyancy on temperature distribution within the bundle. Each fuel rod in the WARD setup has a diameter of 13.18 mm and is arranged with a P/D ratio of 1.08 in a hexagonal duct with a 113.88 mm flat-to-flat distance. Steel wire-wrap spacers, 0.9398 mm in diameter, maintain rod spacing and promote effective coolant flow, with a lead pitch of 101.5 mm. Each rod has a heated length of 1143 mm, designed to mimic typical reactor operating conditions. Table 1 summarizes the design specifications of the WARD 61-pin fuel assembly test section and Fig. 3 shows the radial power distribution within the fuel rod bundle.

3.1.4. KAERI 61-pin assembly

The Korea Atomic Energy Research Institute (KAERI) developed a 61-pin fuel bundle as part of a conceptual design study for the Prototype Generation Sodium-Cooled Fast Reactor (PGSFR) [18]. This experimental setup is a downscaled model of the full-scale 217-pin PGSFR fuel bundle, designed to accurately replicate the original reactor's thermal-hydraulic behavior while preserving essential hydraulic properties. To ensure geometric and hydraulic similarity, the KAERI 61-pin bundle closely matches key parameters of the PGSFR design, including the pitch-to-diameter (P/D) and height-to-diameter (H/D) ratios. This approach ensures that the flow characteristics within the subchannels are representative of those in the larger PGSFR assembly. The fundamental design parameters of this fuel are summarized in Table 1.

3.2. Computational grid system

In the benchmark experiments, thermocouples were used to precisely measure the temperature at key points on the spiral wires, highlighting the importance of accurately representing the wire's helical geometry in simulations. Properly modeling the flow patterns within wire-wrapped fuel bundles is critical for simulating heat transfer mechanisms in SFR fuel assemblies. While most CFD studies and experiments focus primarily on hydraulic behavior, they often overlook the detailed characteristics of heat transfer. Wire-wrapped fuel bundles have complex geometries with numerous points and lines of contact between the pins and wrapping wires, making mesh generation particularly challenging. To overcome this, a novel mesh generation technique was developed using a Fortran-based code [18], which enables the import of highly accurate wire geometries. This approach ensures that the actual wire shape is simulated without distortion, allowing for more precise predictions of the contact area between the wire and the fuel rod. Unlike conventional mesh generation tools, such as those in

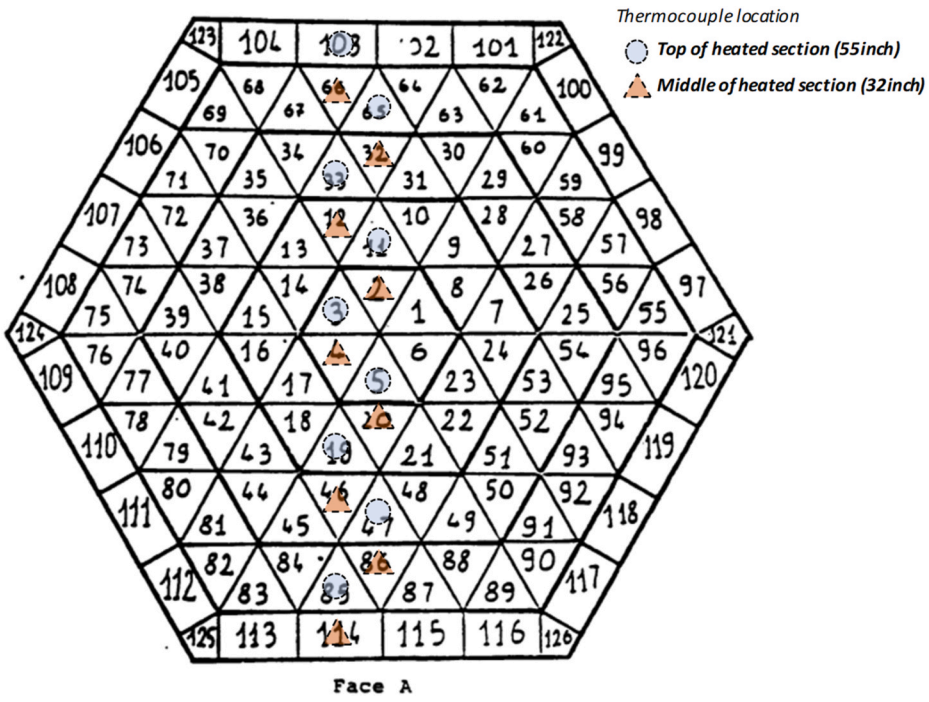

Fig. 3. The WARD 61-pin fuel bundle schematic shows thermocouple locations and subchannel numbers at the top and middle of the heated sections.

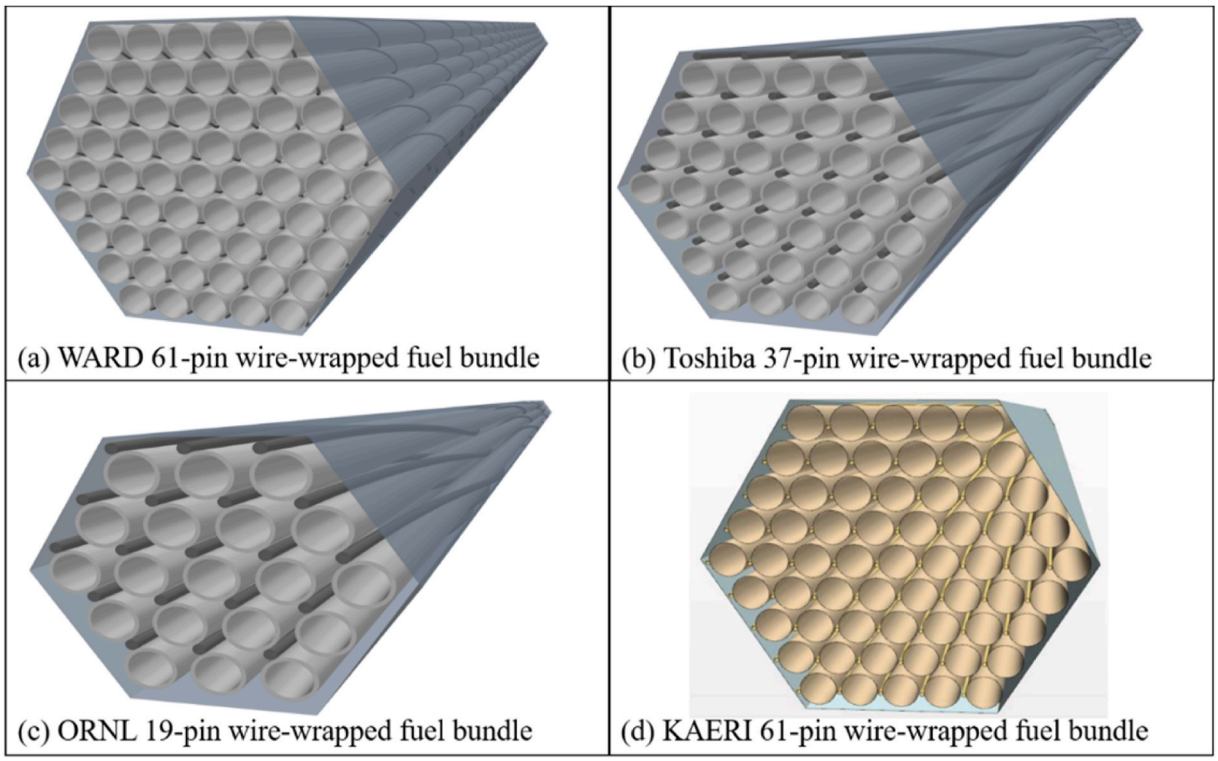

Fig. 4. Perspective view of fuel assemblies used in the study.

STAR-CCM+, this method preserves the true wire shape, improving the accuracy of simulated contact areas. Simulation results demonstrate that this technique accurately predicts pressure drop and flow characteristics [18], and its implementation as a grid-based Reynolds-Averaged Navier-Stokes (RANS) method in CFX has successfully modeled pressure drop and heat transfer in wire-wrapped fuel bundles [19]. The setup distinguishes between the internal fluid domain, formed by the lattice around rods and wire spacers, and the external fluid domain. A conformal fluid-solid mesh interface allows for detailed modeling of heat transfer interactions. This advanced mesh system enables effective analysis of complex heat transfer phenomena in wire-wrapped fuel bundles and achieves convergence even with a limited number of mesh elements. Fig. 4 illustrates the CFD geometry, showing specific configurations for different fuel bundles used in the study. Fig. 5 illustrates an

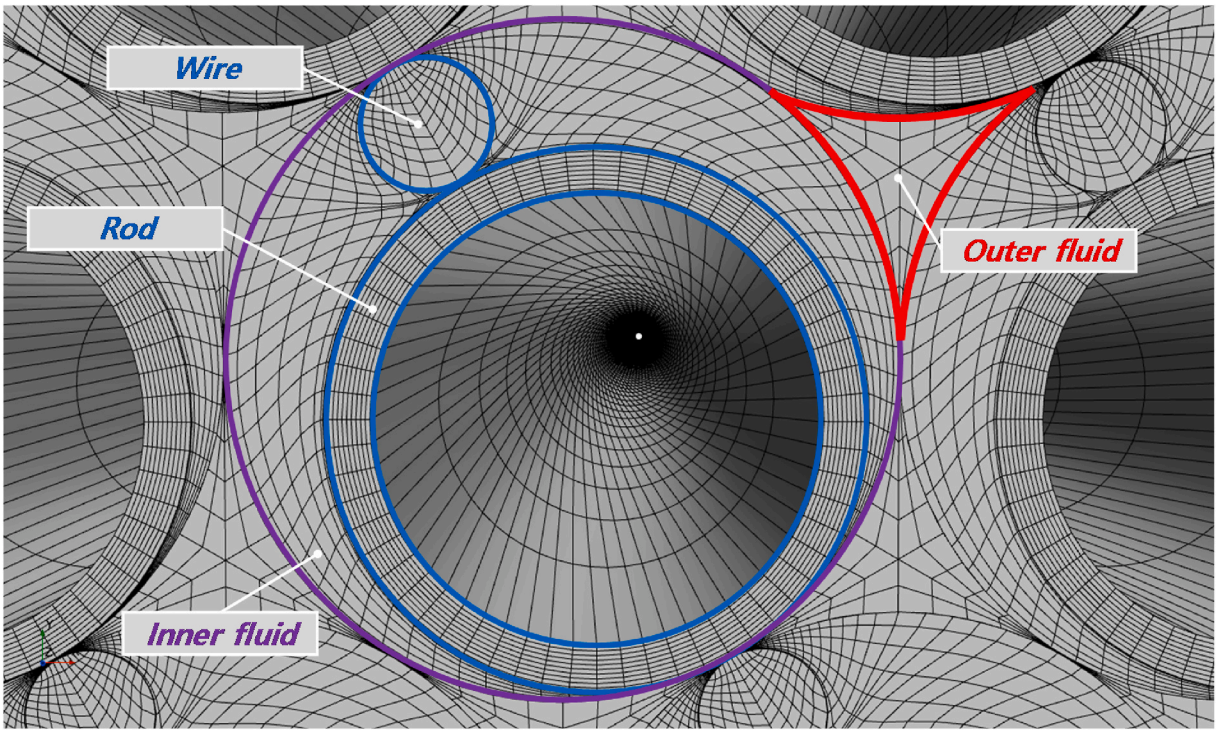

Fig. 5. The computational grid system of the fuel assemblies used in the study (KAERI 61-pin assembly).

innovative grid generation method specifically for the KAERI 61-pin assembly. This assembly was tested solely for hydraulic behavior, without separate domains for rods and wires. It consisted of 26 million hexahedral elements and was utilized in STAR-CCM+ and ANSYS CFX.

3.3. Turbulence models

Turbulent flow fields can be simulated using three primary numerical techniques: Direct Numerical Simulation (DNS), Large Eddy Simulation (LES), and Reynolds-Averaged Navier-Stokes (RANS) simulation. Each technique differs in terms of computational requirements and resolution. For accurate vortex behavior representation in turbulent flows, the grid must be sufficiently fine to either resolve (explicitly capture) or model (approximate) the behavior of vortices at different scales. In DNS, all time and spatial scales of turbulence, including the smallest vortex scales, are directly resolved by solving the governing equations without turbulence modeling. However, due to its extremely high computational cost, DNS is only practical for low Reynolds number flows and simple geometries [20]. In LES, larger vortices (those above the grid scale) are explicitly resolved, while smaller vortices below the grid scale are approximated using a sub-grid-scale (SGS) model [21]. LES is computationally more efficient than DNS but still demands significant resources, limiting its feasibility for complex engineering applications. In contrast, RANS is widely used in engineering due to its lower computational cost. RANS solves time-averaged Navier-Stokes equations and approximates the effects of turbulence using turbulence models, which compute the Reynolds stress tensor resulting from turbulent momentum fluctuations. While RANS does not resolve individual vortex structures, it effectively models turbulence behavior for complex and practical applications without requiring highly refined grids [20,21].

ANSYS CFX and STAR-CCM + offer various built-in turbulence models, including the k-ε, k-ω, Reynolds Stress, and Spalart-Allmaras models, each with strengths suited to specific flow conditions. The **k-ε model** performs well in predicting free turbulence in low-pressure gradient areas but struggles with boundary layer separation in near-wall regions and under large adverse pressure gradients. In contrast, **Wilcox's k-ω model** excels in near-wall regions and accurately predicts separation caused by reverse pressure gradients but is highly sensitive to incoming turbulence levels [22,23]. To address these limitations, **Menter's SST (Shear Stress Transport) model** was developed, combining the strengths of both k-ε and k-ω models [24,25]. Specifically, the SST model uses the k-ε formulation in free-stream regions and transitions to the k-ω formulation near walls, making it robust for handling wall-bounded turbulent flows.

3.4. Sensitivity studies of wall grid scales and turbulence models

In the previous study, a sensitivity analysis of turbulence models k-ε, k-ω, and SST was performed using **ANSYS CFX solver** [18]. The results showed that the friction factors from the SST model were 0.9 %–2.6 % higher than those from the k-ε model and 0.9 %–3.8 % lower than those from the k-ω model. Thus, the SST model's friction factor falls between the values from the k-ε and k-ω models. To capture the transition from laminar to turbulent flow on the fuel rod surface, a minimum grid scale of $\mathbf{5.0 \times 10^{-7}}$ **mm** was used, achieving a y^+ value of approximately 2.5. The SST turbulence model was selected for this CFD analysis as it effectively balances resolution and computational efficiency, capturing both turbulent flow and heat transfer characteristics in SFR fuel bundles. Among the turbulence models tested, the k-ε model produced higher turbulent kinetic energy (TKE), enhancing thermal mixing caused by wire spacers. This resulted in more efficient thermal mixing across the system compared to other models. The differences in TKE predictions between the k-ε and k-ω models are primarily attributed to variations in their production terms [26]. For clarity, the transport equations for the **k-ε** and **k-ω** models are presented below:

For the k-ε model:

$$\frac{\partial}{\partial t}(\rho k) + \nabla \cdot (\rho k \, \overline{\boldsymbol{v}}) = \nabla \cdot \left[\left(\mu + \frac{\mu_t}{\sigma_k} \right) \nabla k \right] + P_k - \rho(\varepsilon - \varepsilon_0) + S_k \tag{1}$$

$$\frac{\partial}{\partial t}(\rho \varepsilon) + \nabla \cdot (\rho \varepsilon \, \overline{\boldsymbol{v}}) = \nabla \cdot \left[\left(\mu + \frac{\mu_t}{\sigma_\varepsilon} \right) \nabla \varepsilon \right] + \frac{1}{T_e} C_{\varepsilon 1} P_\varepsilon - C_{\varepsilon 2} f_2 \rho \left(\frac{\varepsilon}{T_e} - \frac{\varepsilon}{T_0} \right) + S_\varepsilon \tag{2}$$

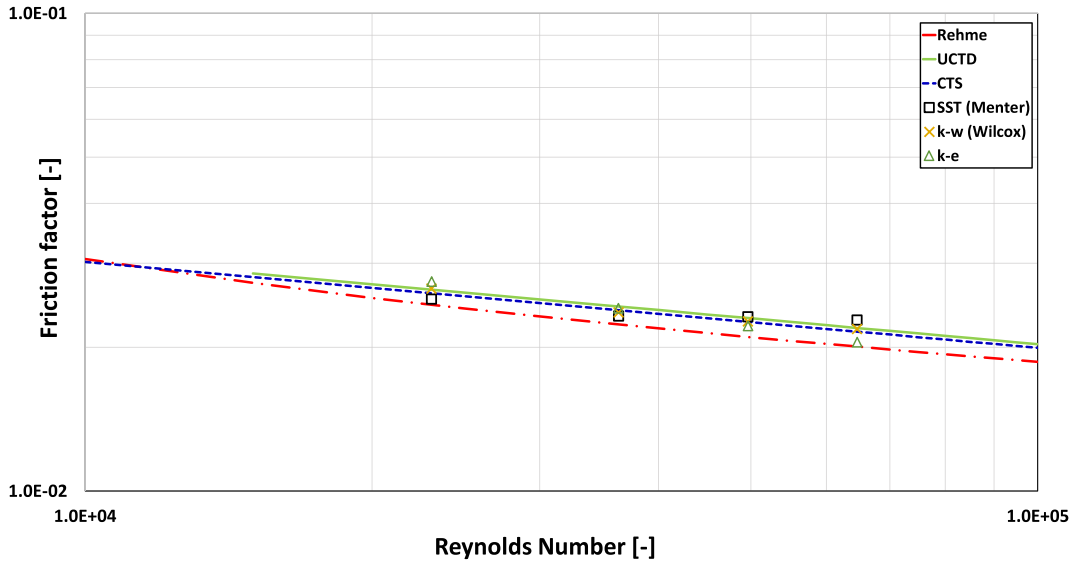

Fig. 6. Comparison of friction factors for KAERI 61-pin fuel bundle using different turbulence models.

For the k-ω model:

$$\frac{\partial}{\partial t}(\rho k)+\nabla\cdot(\rho k\,\overline{\boldsymbol{v}})=\nabla\cdot[(\mu+\sigma_k\mu_t)\nabla k]+P_k-\rho\beta^* f_{\beta^*}(\omega k-\omega_0 k_0)+S_k \tag{3}$$

$$\frac{\partial}{\partial t}(\rho\omega)+\nabla\cdot(\rho\omega\,\overline{\boldsymbol{v}})=\nabla\cdot[(\mu+\sigma_k\mu_t)\nabla\omega]+P_\omega-\rho\beta f_\beta(\omega^2-\omega_0^2)+S_\omega \tag{4}$$

Here, P_k is the production of turbulent kinetic energy due to shear strain, and P_ε represents the production of the dissipation rate. Variations in production terms distinguish different model formulations, such as the Standard and Realizable k-ε models. These terms account for effects like buoyancy production (G_b) and compressibility modifications (γ_M):

For the Standard k-ε model:

$$P_k = G_k + G_{nl} + G_b - \gamma_M \tag{5}\text{-}1$$

$$P_\varepsilon = G_k + G_{nl} + C_{\varepsilon 3}G_b \tag{5}\text{-}2$$

For the Realizable k-ε model:

$$P_k = f_c G_k + G_b - \gamma_M \tag{5}\text{-}3$$

$$P_\varepsilon = f_c S_k + C_{\varepsilon 3}G_b \tag{5}\text{-}4$$

Here, G_k is turbulent production, G_{nl} is non-linear production, G_b is buoyancy production, and γ_M represents compressibility modification. where:

$$G_k = \mu_t S^2 - \frac{2}{3}\rho k\nabla\cdot\overline{v} - \frac{2}{3}\mu_t(\nabla\cdot\overline{v})^2$$

$$G_b = \beta\frac{\mu_t}{Pr_t}(\nabla\overline{T}\cdot g)$$

$$G_{nl} = \nabla\cdot\overline{v}$$

$$\gamma_M = \frac{\rho C_M k\varepsilon}{c^2}$$

Similarly, the SST k-ω model modifies these terms, introducing specific dissipation production (G_ω) and cross-diffusion (D_ω), for enhanced performance in diverse flow regimes. The production terms for the SST k-ω model are formulated as follows:

For the **Standard k-ω model**:

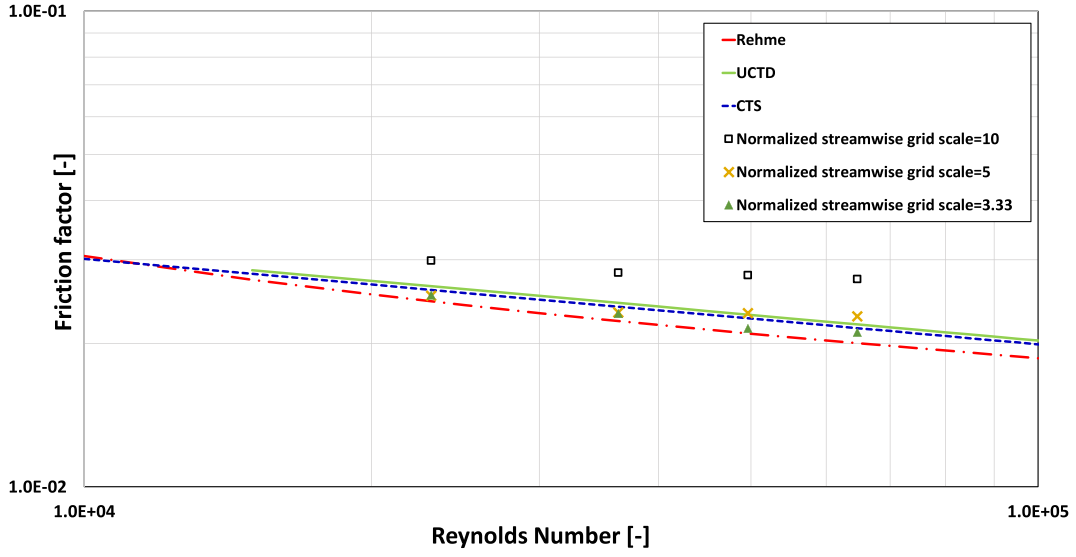

Fig. 7. Influence of axial grid spacing on friction factor predictions for KAERI 61-pin fuel bundle.

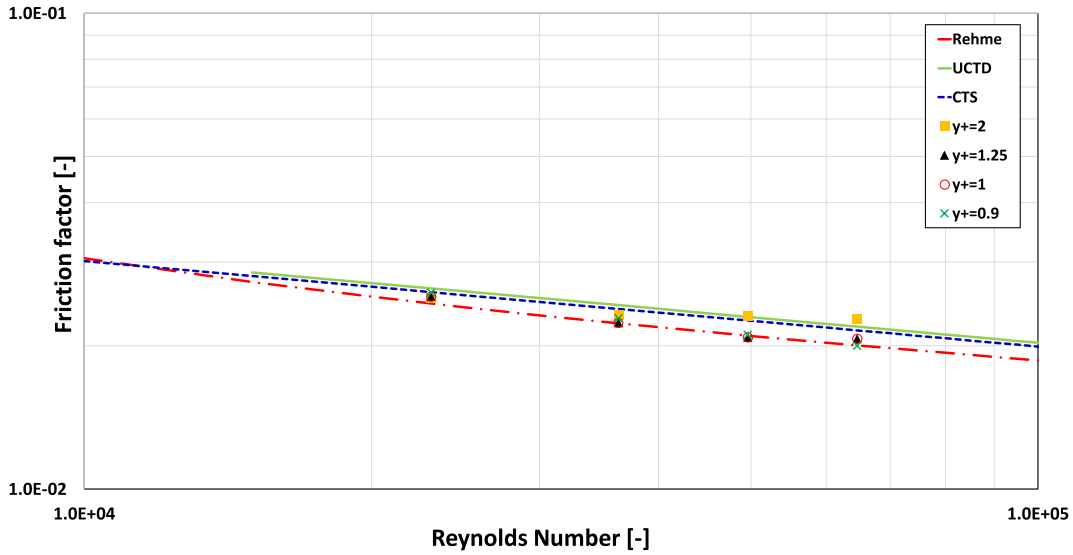

Fig. 8. Effect of Wall-Normal Grid Spacing (y+) on Friction Factor Predictions for KAERI 61-Pin Fuel Bundle (Grid sensitivity test result).

$$P_k = G_k + G_b \quad (5)\text{-}5$$

$$P_\omega = G_\omega \quad (5)\text{-}6$$

For the **SST k-ω model**:

$$P_k = G_k + G_{nl} + G_b \quad (5)\text{-}7$$

$$P_\omega = G_\omega + D_\omega \quad (5)\text{-}8$$

Here, G_ω is Specific dissipation production and D_ω is a Cross-diffusion term. where:

$$G_k = \mu_t f_c S^2 - \frac{2}{3}\rho k \nabla\cdot\bar{v} - \frac{2}{3}\mu_t(\nabla\cdot\bar{v})^2$$

$$G_b = \beta\frac{\mu_t}{Pr_t}(\nabla\bar{T}\cdot g)$$

$$G_{nl} = \nabla\cdot\bar{v}$$

$$G_\omega = \begin{cases} Standard\ k-\omega : \rho\alpha\left[\left(\alpha^* S^2 - \frac{2}{3}(\nabla\cdot\bar{v})^2\right) - \frac{2}{3}\omega\nabla\cdot\bar{v}\right] \\ SST\ k-\omega : \rho\gamma\left[\left(S^2 - \frac{2}{3}(\nabla\cdot\bar{v})^2\right) - \frac{2}{3}\omega\nabla\cdot\bar{v}\right] \end{cases} \text{ and}$$

$$D_\omega = 2\rho(1-F_1)\sigma_{\omega_2}\frac{1}{\omega}\nabla k\cdot\nabla\omega$$

These modifications enable the SST model to resolve complex flow and thermal patterns in wire-wrapped fuel bundles accurately, making it particularly suited for the current study.

The current study focused on analyzing the sensitivity of STAR-CCM + to three turbulence models: k-ε, k-ω, and SST. The results were compared to experimental correlations, including the Rehme correlation [27], the Upgraded Cheng and Todreas Detailed (UCTD) correlation [28], and the Cheng and Todreas Simple correlation (CTS) [29]. Fig. 6 presents the CFD results for each model against the friction factor of the KAERI 61-pin fuel bundle. Across all Reynolds numbers, the error margin for all turbulence models with the UCTD correlation remained within 5 %, with the **k-ω** and **SST models** providing the highest accuracy under actual operating conditions.

Further grid sensitivity studies were conducted to analyze the impact of axial grid spacing and wall-normal grid spacing (y+) on the simulation results. Figs. 7 and 8 illustrate the effects of varying y + values and streamwise grid spacings on friction factor predictions for the KAERI 61-pin fuel bundle. Specifically, y + influences the calculation of the specific dissipation rate in the k-ω model, with finer grids (e.g., y+ = 1.25) providing improved accuracy. Comparisons of different streamwise and radial grid spacings revealed that coarser axial grids increased discretization errors, particularly in pressure drop predictions, where a normalized streamwise grid scale of 10 produced inaccurate results. **To minimize these errors, a denser axial grid with a normalized streamwise grid scale of 5 was adopted as a practical compromise between computational efficiency and accuracy.**

In this study, the SST turbulence model was chosen for CFD analysis due to its balanced performance and ability to resolve wall-bounded flows accurately. The grid resolution was set to a y^+ value of 2 and a normalized streamwise grid scale of 5, which enabled detailed investigations of 3-dimensional and vortical flow phenomena using both STAR-CCM+ and ANSYS CFX. Additionally, to capture the transition from laminar to turbulent flow on the surface of the fuel rod, the near-wall grid scale was set to 5.0×10^{-7} m, ensuring the friction velocity parameter (y^+) remained close to 1. This fine-grid resolution is critical for resolving near-wall turbulence behavior while maintaining computational efficiency. A high-resolution scheme was applied to the convective term, and convergence was ensured by monitoring periodic pressure variations at the outlet domain of the 61-pin fuel bundle. **The CFD results that most closely aligned with experimental data were used to study the flow behavior in detail.** Based on the findings from the grid sensitivity studies, additional analyses were carried out on the ORNL 19-pin and Toshiba 37-pin fuel bundles to evaluate the effects of different turbulence models. As shown in Fig. 9, the CFD results demonstrated excellent agreement with the UCTD model, confirming the suitability of the SST turbulence model for accurate simulation under these conditions.

Therefore, in this study, steady-state RANS simulations were conducted using the SST turbulence model. The computational grid was configured with a y^+ value of 2 (ensuring near-wall resolution) and a normalized streamwise grid scale of 5 to resolve three-dimensional flow structures and vortical phenomena in STAR-CCM+ and ANSYS CFX. A high-resolution numerical scheme was employed for the discretization of convective terms. Simulation convergence was determined by monitoring periodic pressure fluctuations at the outlet of the 61-pin fuel assembly. Furthermore, CFD results exhibiting the closest agreement with experimental data were prioritized to analyze and interpret the underlying flow mechanisms effectively.

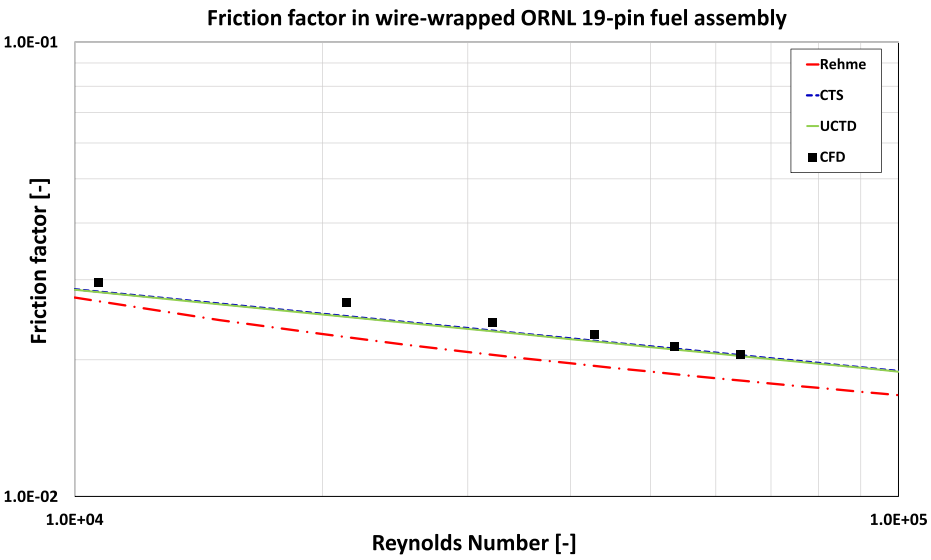

(a) Friction factor in ORNL 19-pin bundle

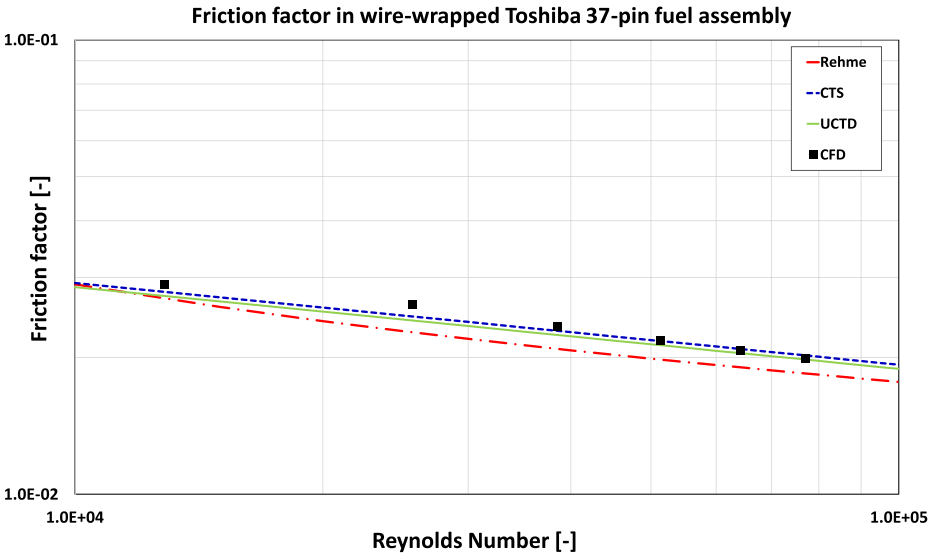

(b) Friction factor in Toshiba 37-pin bundle

Fig. 9. Pressure drop comparison of CFD results and experimental correlations for ORNL 19-pin and Toshiba 37-pin fuel bundles.

3.5. Code-to-code validation using KAERI 61- pin data

To validate the STAR-CCM + analysis results, a code-to-code comparison was performed with ANSYS CFX. Both solvers employed the same boundary conditions and mesh configurations to ensure consistency. Previous studies have demonstrated the reliability of ANSYS CFX for high-fidelity CFD analyses of fuel bundles with varying pin counts, including 7, 19, 37, 61, 127, and 217 pins, validated against experimental data and established friction factor correlations [18]. In this study, the verified ANSYS CFX results served as the reference for comparison with **STAR-CCM + simulations**. While both solvers used similar inputs, differences in automatic grid generation led to variations in mesh element types, which could impact numerical accuracy. Both solvers relied on the SST turbulence model to predict flow dynamics and pressure drops in the KAERI 61-pin fuel bundle.

Table 2
Application range and database for friction factor correlations.

Model	N_r	P/D	H/D	Reynolds number range	Uncertainty
Rehme	7–217	1.1–1.42	8.0–50.0	1000–3 × 10^5	±8 %
Engel	19–61	1.067–1.082	7.7–8.3	All regimes (50-10^6)	±15 %
CTS	19–217	1.025–1.420	8.0–50.0	All regimes (50-10^6)	Not evaluated
UCTD	7–271	1.000–1.420	8.5–52.0	All regimes (50-10^6)	Not evaluated

3.5.1. Comparison of pressure drop

Pressure drops across the KAERI 61-pin bundle were predicted using STAR-CCM+ and ANSYS CFX and validated against experimental data and widely used friction factor correlations, including those by Rehme [27], Engel [30], and Cheng and Todreas (CTS and UCTD) [28,29].

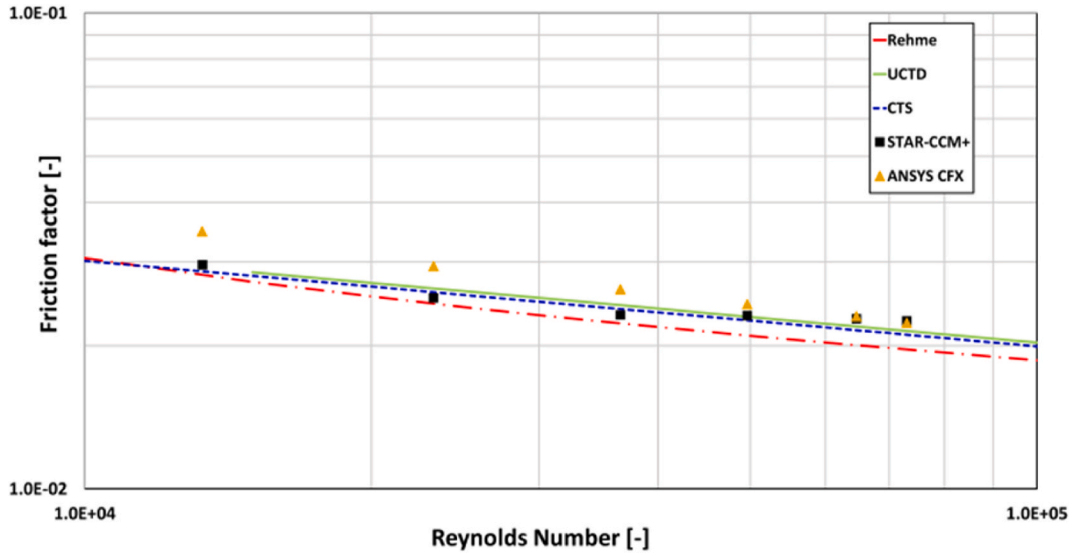

Fig. 10. Friction factors with different CFD code.

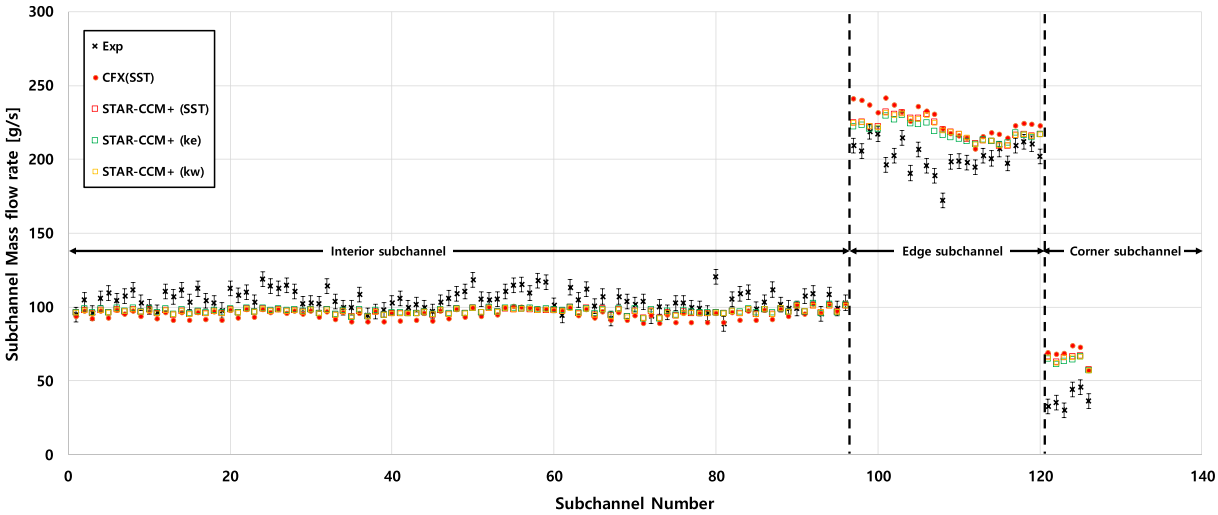

Fig. 11. Comparison of subchannel mass flow rate predictions for KAERI 61-pin bundle.

These correlations consider various parameters such as Reynolds number, bundle geometry, and wire-wrap characteristics. The validity range of each correlation is summarized in Table 2. It is essential to select the appropriate correlation equation to accurately represent the behavior of SFR fuel rods. In this study, the pressure drop predictions from STAR-CCM+ and ANSYS CFX for the KAERI 61-pin bundle were compared against experimental data and these correlations.

Fig. 10 compares the CFD results for the 61-pin fuel assembly with established friction factor correlations. The CFD predictions align most closely with the UCTD correlation, which is widely recognized for its accuracy in modeling pressure drop behavior in wire-wrapped fuel rod bundles. At nominal operating flow conditions (Reynolds number, $Re \approx$ 65,000), ANSYS CFX and STAR-CCM + overestimate the UCTD correlation by approximately 4 %. However, under low-flow-rate conditions, significant deviations from experimental correlations are observed, likely due to transitional flow regimes that challenge the predictive capability of standard turbulence models. Experimental data at the same flow rate recorded a pressure drop of 0.488 MPa [31], while the CFD simulations yielded 0.500 MPa, corresponding to a marginal error of 2.4 %. This discrepancy highlights the limitations of current turbulence models in capturing complex flow transitions at reduced flow rates, underscoring the need for further refinement in low-flow predictive methodologies. Both solvers produced comparable results, confirming their ability to accurately simulate pressure drops in wire-wrapped bundles. Minor differences between the solvers were attributed to variations in mesh structure and solver-specific numerical algorithms.

3.5.2. *Comparison of subchannel mass flow rate*

Accurate prediction of subchannel mass flow rates is critical for understanding flow distribution in wire-wrapped fuel bundles. In this study, experimental data for the KAERI 61-pin bundle, obtained using an iso-kinetic sampling method, were compared with CFD predictions from STAR-CCM+ and ANSYS CFX to evaluate their performance. Subchannel positions and numbers were consistent with reference [32], ensuring accurate comparisons between CFD and experimental results. These comparisons are illustrated in Fig. 11, which shows the flow distribution across interior, edge, and corner subchannels. For interior subchannels, the CFD predictions showed strong agreement with experimental data from Ref. [32], with an absolute error of 7.63 % for STAR-CCM+ and 9.34 % for ANSYS CFX. This consistency highlights the capability of both solvers to accurately capture flow behavior in regions where flow interactions are uniform and less influenced by boundary effects. The

Table 3
Relative differences between CFD predictions and experimental data for subchannel mass flow rates in the KAERI 61-Pin bundle.

Subchannel Type	Experiment [g/s]	Experimental Uncertainty (%)	CFD STAR-CCM + [g/s]	CFD ANSYS CFX [g/s]	STAR-CCM + Absolute Error (%)	ANSYS CFX Absolute Error (%)
Interior	104.9	2.53	96.9	95.1	7.63	9.34
Edge	202.1	2.53	220.5	225.8	9.10	11.73
Corner	37.4	2.53	64.2	68.1	71.66	82.09

Note: Error = (CFD−EXP)/EXP × 100 %.

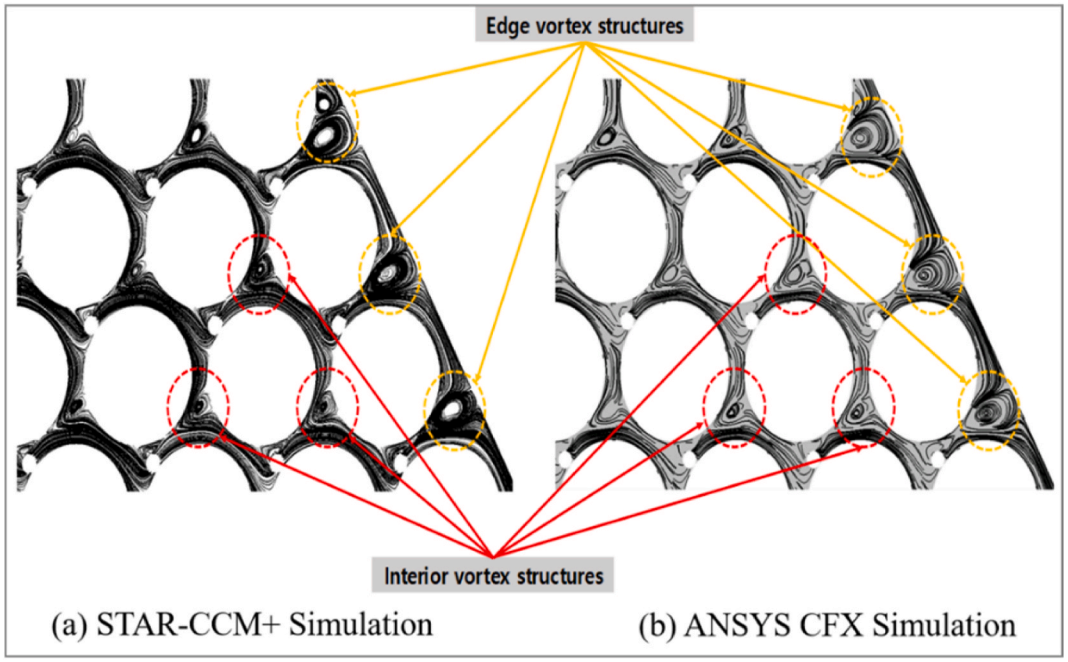

Fig. 12. Comparison of vorticity distribution predicted by CFD codes in the intermediate section of the KAERI 61-Pin Fuel Assembly.

findings align with those in Ref. [7], where the minimal influence of turbulence models on inter-subchannel mass flow differences was observed in the 37-pin bundle. Similarly, this study demonstrates that the SST turbulence model used in both solvers is robust for predicting interior subchannel flow distributions.

The differences in mass flow rate predictions between STAR-CCM+ and ANSYS CFX, despite both using the SST turbulence model, can be attributed to several factors. First, variations in grid generation techniques and numerical discretization schemes result in differences in mesh quality and resolution, particularly in complex flow regions such as edge and corner subchannels. Each solver employs proprietary algorithms for solving the Navier-Stokes equations, leading to differences in SST model implementation, including blending functions and wall treatment strategies. Additionally, the application of boundary conditions (particularly near walls) further contributes to discrepancies, as STAR-CCM+ and ANSYS CFX may handle flow transitions differently.

While both STAR-CCM+ and ANSYS CFX performed well in analyzing interior subchannels, discrepancies were noted in the edge and corner subchannels, as shown in Fig. 11. For the **edge subchannels**, STAR-CCM + exhibited an error of 9.10 %, while ANSYS CFX had a slightly higher error of 11.73 %. This overprediction aligns with the localized flow acceleration observed near the duct walls, which is challenging to model accurately. In the corner subchannels, the largest discrepancies were recorded, with STAR-CCM + showing an error of 71.66 % and ANSYS CFX displaying an error of 82.09 %. These significant deviations are likely attributed to small geometric uncertainties, such as slight misalignments in rod positioning during testing, [32], which substantially impacts localized flow patterns in these regions. Table 3 highlights the absolute percentage errors for subchannel types, showing that STAR-CCM + had better accuracy, especially for interior subchannels. Both solvers effectively predicted mass flow rates for interior regions, aligning well with experimental results. However, discrepancies in edge and corner subchannels reveal challenges in modeling localized flow and the need for precise geometry. Fig. 11 reinforces these findings and points to areas for improvement in peripheral subchannels.

3.5.3. *Comparison of flow phenomena using vortical structures*

Understanding the flow phenomena in wire-wrapped fuel bundles is essential for predicting their thermal-hydraulic performance, particularly the effects of vortical structures from the wire wraps. This analysis compares the STAR-CCM+ and ANSYS CFX simulations, both employing a high-resolution scheme and the SST turbulence model, to evaluate their effectiveness in capturing flow characteristics that impact performance. Using critical point theory, we identified vortex structures and their relationship to flow behaviors in each subchannel [18]. As illustrated in Fig. 12, the edge, corner, and interior vortex structures vary periodically with the relative positions of the wire spacer and duct wall. Edge vortices exhibit higher axial velocities and form larger longitudinal vortex structures compared to the other subchannels. This strong longitudinal vortex structure in the edge subchannel enhances heat transfer relative to the corner and interior subchannels. The CFD analysis in STAR-CCM+ and ANSYS CFX captured these vortex structures effectively. However, differences in vortex intensity were noted; STAR-CCM + exhibited more defined vortex cores, while ANSYS CFX showed slightly diffused structures. Despite these variations, both solvers successfully captured the overall dynamics of the vortices and resolved secondary flow patterns crucial for fluid mixing and heat transfer.

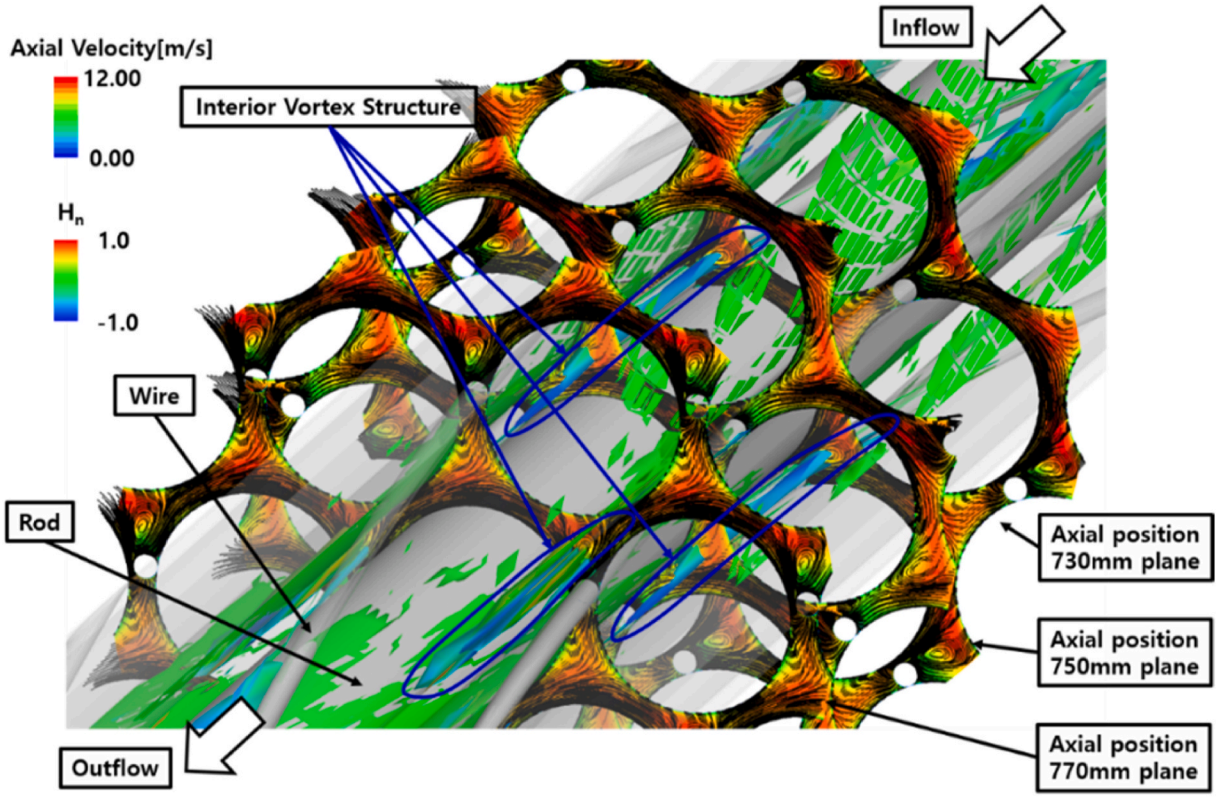

(a) Interior subchannel

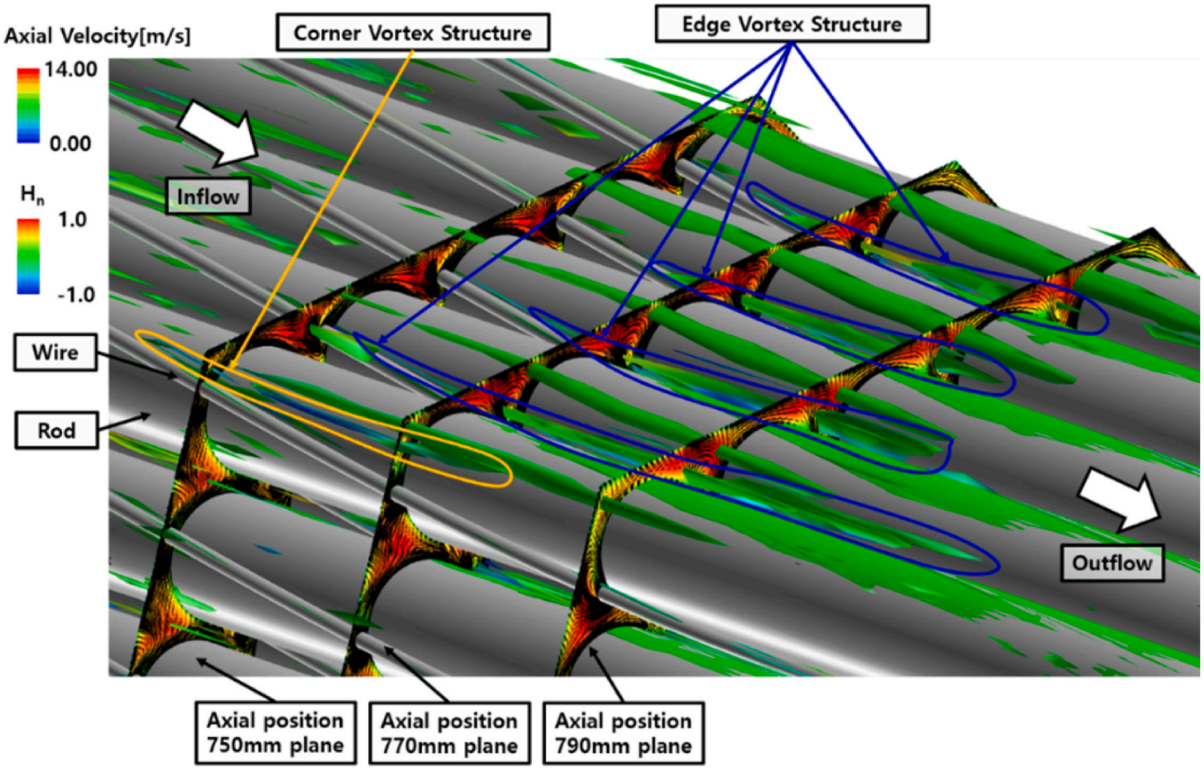

(b) Edge and Corner subchannel

Fig. 13. Visualization of vortex core distribution and vorticity within the KAERI 61-Pin Fuel Assembly, illustrating periodic changes in vortex structures.

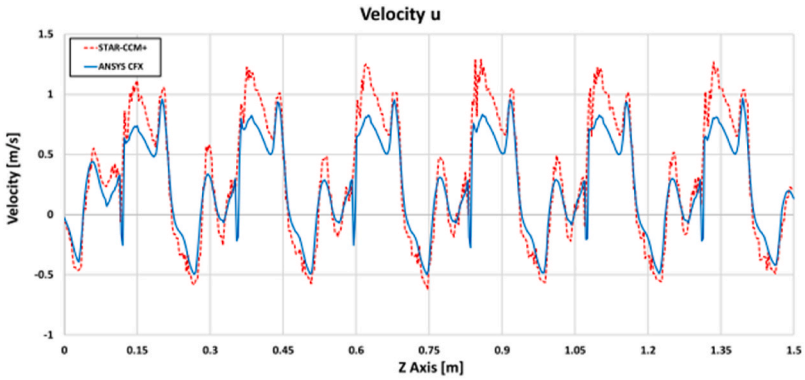

(a) Velocity u of each CFD code at point

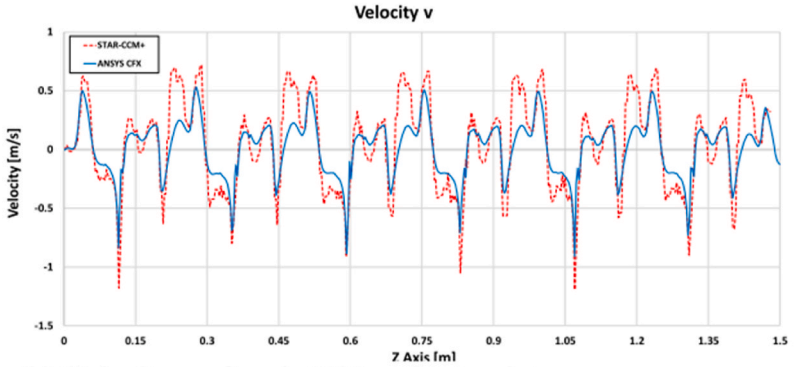

(b) Velocity v of each CFD code at point

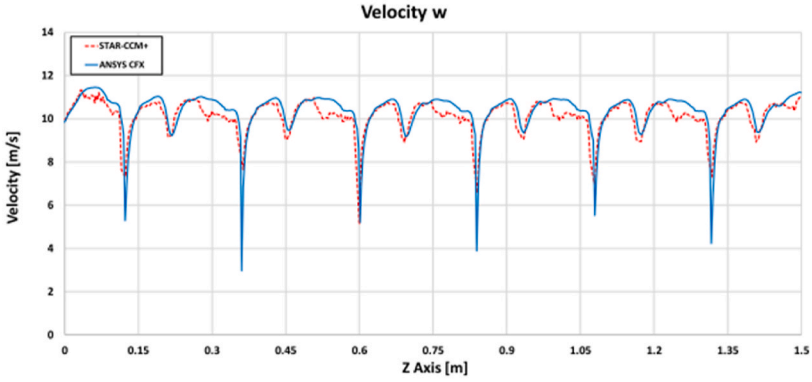

(c) Velocity w of each CFD code at point

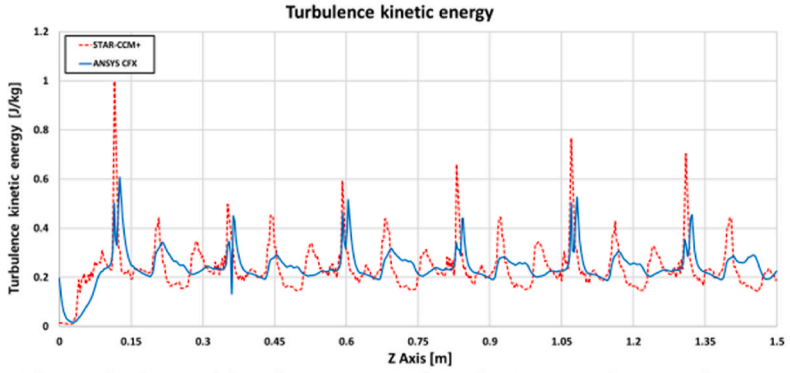

(d) Turbulence kinetic energy of each CFD code at point

Fig. 14. Comparison of velocity components and turbulence kinetic energy.

Using Sawada's vortex identification method, developed in 1995 [33], vortex structures were visualized by coloring the vortex core with normalized helicity to indicate rotation direction. The normalized helicity (H_n) is defined as:

$$H_n = \frac{\vec{\zeta} \cdot \vec{\omega}}{|\zeta| \cdot |\omega|} \quad (6)$$

where ζ is the absolute vorticity vector and ω the relative velocity vector. This parameter offers insights into the rotational direction, where $H_n > 0$ indicates rotation and axial movement following the right-hand rule, $H_n = 0$ indicates stagnation or rotation without axial movement, and $H_n < 0$ indicates rotation following the right-hand rule with movement opposite the axial direction. Fig. 13 illustrates the vortex structures within each subchannel, highlighting their periodic variations as the wire spacer's position changes relative to the duct wall. These periodic changes in vortex structure are consistent with the observations discussed earlier in this section. Both STAR-CCM+ and ANSYS CFX successfully capture these periodic vortex behaviors and their relationship to flow dynamics, demonstrating their reliability for analyzing complex geometries like wire-wrapped fuel bundles. This reinforces confidence in the applicability of these commercial CFD tools for thermal-hydraulic simulations.

To further analyze solver-specific differences in flow phenomena, Fig. 14 compares the axial velocity components and turbulent kinetic energy (**TKE**) distributions between STAR-CCM+ and ANSYS CFX simulations in the **interior subchannel** of the KAERI 61-pin bundle. The axial velocity profiles in both solvers exhibit nearly identical trends, with periodic low-speed regions emerging downstream of the wire spacer wake at peak points. However, **minor discrepancies** were observed in the transverse velocity components (**u and v**), with STAR-CCM + predicting slightly higher transverse velocity fluctuations. These differences correlate with **higher turbulent kinetic energy predictions in STAR-CCM + compared to ANSYS CFX**, particularly near the wire-wrapped regions where secondary flows are dominant. The enhanced TKE distribution in STAR-CCM + suggests a stronger capture of flow instability and secondary motion effects, which could contribute to improved thermal mixing. This difference aligns with previously observed variations in solver-specific SST turbulence model implementations, where blending functions and near-wall treatment strategies impact flow resolution and turbulence intensity.

These findings underscore the influence of solver-specific numerical formulations on predicting vortex-induced flow structures. While both solvers effectively capture large-scale vortices, STAR-CCM + tends to predict more intense turbulence characteristics, particularly in regions where wire-wrap interactions induce secondary flow structures. The **higher TKE distribution in STAR-CCM +** , as depicted in Fig. 14, suggests that it resolves smaller-scale turbulent eddies more effectively than ANSYS CFX. However, this also raises potential concerns regarding numerical diffusion effects in STAR-CCM+ and their influence on long-range turbulence transport. Further refinement of turbulence models and numerical schemes may be required to improve consistency between solvers, particularly in regions of flow recirculation and transition.

4. Heat transfer result

The code-to-code comparisons conducted in Section 3 demonstrated strong agreement between the predicted results from STAR-CCM+ and ANSYS CFX, with STAR-CCM + exhibiting closer alignment with experimental data in most cases. This section presents an evaluation of the heat transfer characteristics essential for managing fuel bundle temperatures using high-fidelity STAR-CCM + CFD simulations. A comparative analysis is conducted between CFD-predicted temperature distributions and experimental data for three specific fuel bundle configurations: the ORNL 19-pin, Toshiba 37-pin, and WARD 61-pin assemblies. To ensure accuracy, validated turbulence models and detailed meshing techniques are employed to capture the complex thermal and flow behaviors within these assemblies. By comparing simulation results with experimental observations, the computational models are verified, providing insights into key heat transfer mechanisms and identifying potential improvements in simulation accuracy and thermal management strategies.

Table 4
Experiment condition of the ORNL 19-pin, Toshiba 37-pin, and WARD 61-pin bundles.

Experimental fuel bundle	Test No. (Run No.)	Inlet Temp. [°C]	Flow rate [kg/s]	Power [kW]	Skew [Max/Min]
ORNL 19-Pin	Test 2. (109)	315.55	2.932	166.25	1.0:1
	Test 3. (101)	315.55	2.932	166.25	1.2:1
	Test 6. (102)	315.55	2.172	332.5	1.0:1
	Test 14. (101)	315.55	2.932	166.25	3:1
Toshiba 37-Pin	E37P02	211.3	1.612	53.58	1.0:1
	C37P06	203.5	0.374	41.02	
	E37P13	206.4	0.105	13.40	
	E37P17	209.5	1.096	53.82	1.17:1
	E37P20	204.6	0.358	53.82	
	F37P27	204.5	0.195	32.56	
	G37P22	205.8	1.074	54.57	1.34:1
	G37P25	203.7	0.358	54.57	
	L37P43	205.1	0.163	34.13	
WARD 61-Pin	Test 223	315	2.005	260	2.8:1
	Test 226	315	2.005	260	1.0:1
	Test 403	315	2.005	264	2.0:1

Table 5
Boundary conditions for CFD analysis.

Boundary Domain	Condition	Value
Inlet	Constant velocity	Various
Outlet	Relative pressure	0 Pa
Rod outer/Wire outer	No slip (Smooth wall)	–
Duct wall	No slip (Adiabatic)	–
Heat source (clad inner surface)	Constant heat flux	Various

4.1. Computational Boundary Conditions

The CFD analysis used experimental data from the ORNL 19-pin, Toshiba 37-pin, and WARD 61-pin bundles with simulation parameters carefully aligned with experimental conditions as detailed in Table 4. The inlet boundary conditions were defined by varying mass flow rates to simulate different operational scenarios, and heat flux boundary conditions were applied to the inner cladding surfaces of the heated section, calibrated to reflect experimental thermal conditions. Heat generation varied between pins, with the specific distribution of heat (power skew) illustrated in Figs. 1–3.

During CFD Analysis, a 0 Pa pressure boundary was set at the outlet to simulate an unobstructed exit, while a no-slip condition with smooth surface roughness was applied to the surfaces of the rods and wire spacers to accurately capture fluid dynamics. The duct walls were modeled with no-slip, adiabatic conditions, assuming smooth surface interaction without heat transfer through the walls, ensuring thermal insulation. A summary of the Computational Boundary conditions is given in Table 5. The CFD methodology was validated previously using the KAERI 61-pin assembly, as discussed in the preceding section 4.2. A turbulent Prandtl number (Prt) of 0.02, previously validated, was adopted for these simulations [14].

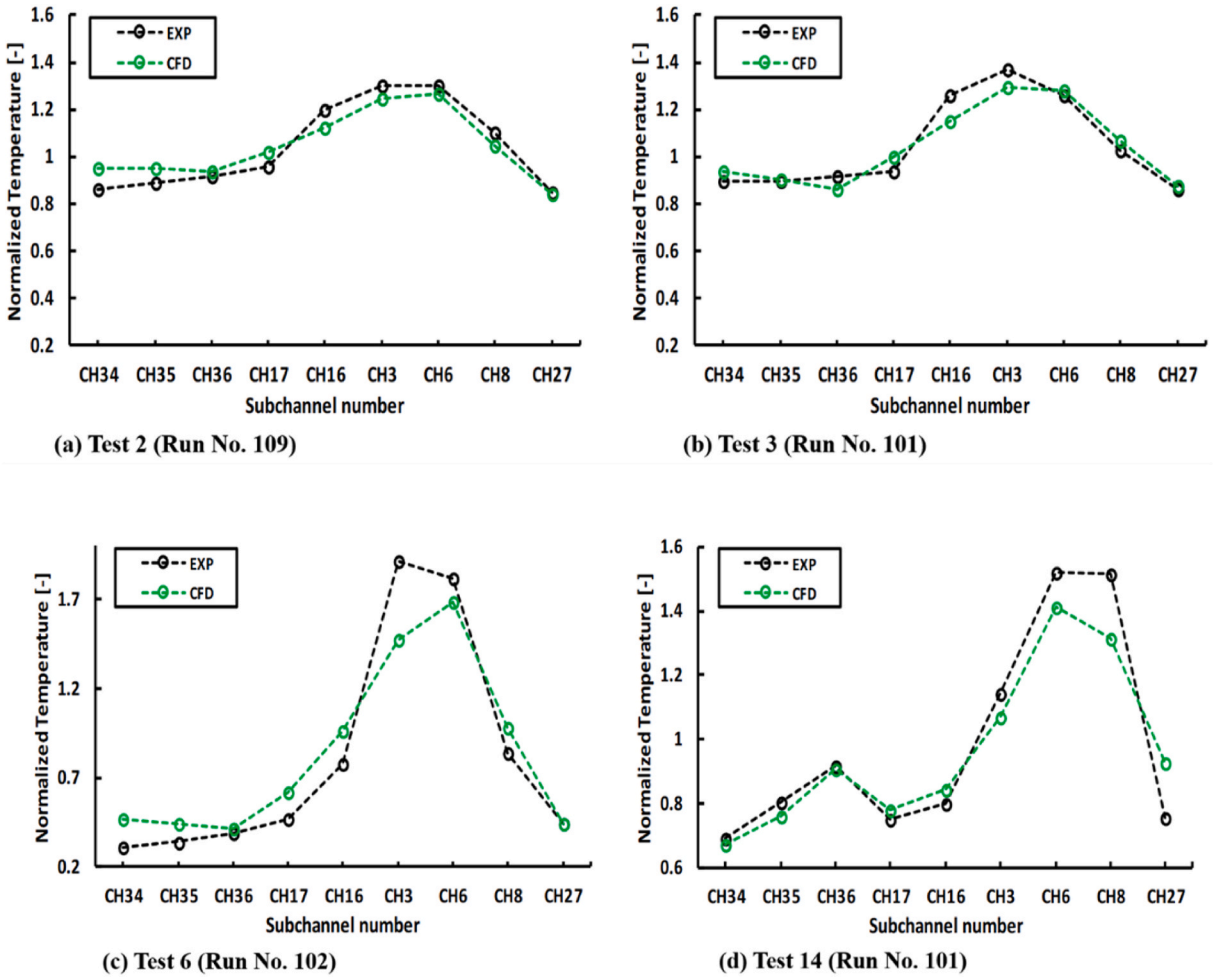

Fig. 15. Comparison of experimental results with CFD results for ORNL 19-pin fuel bundle.

4.2. Validation of experimental and CFD results

4.2.1. ORNL 19-pin configuration

The validation of the ORNL 19-pin configuration involved temperature verification at multiple subchannels (CH3, CH6, CH8, CH16, CH17, CH27, CH34, CH35, and CH36) using outlet data from experiments and CFD simulations. Four test scenarios, detailed in Table 4, varied flow rates, bundle power, and heating patterns to evaluate the thermal response and accuracy of the computational model. Fig. 15 compares experimental and CFD results across these tests, illustrating the varying degrees of accuracy, while Fig. 16 shows the temperature contours at the bundle outlet, highlighting the impact of heating patterns on thermal distribution.

In **Test 2**, where all pins were uniformly heated, the CFD and experimental results exhibited minimal discrepancies, with a maximum error of 10.8 % at subchannel CH34. This outcome demonstrated the model's robustness in predicting uniform heat transfer trends. In **Test 3**, a mild heat skew (1.2:1) was applied, resulting in a maximum error of 8.5 % at CH16. The agreement between CFD and experimental trends indicated reasonable predictive accuracy for small heat gradients.

In **Test 6**, where only pins 1–7 were heated, significant non-uniformities arose in the thermal field. This scenario exhibited the largest discrepancies, with a maximum error of 23.0 % at CH3. These errors were attributed to the challenges of capturing complex turbulent heat transfer under highly localized heating conditions. In **Test 14**, a substantial heat skew (3:1) was applied to specific pins, leading to considerable temperature variations among subchannels. The maximum error reached 24.5 % at CH27, underscoring limitations in turbulence modeling under extreme heat flux gradients. These findings emphasize the critical need for precise turbulence models and accurate boundary condition specifications, particularly for scenarios involving non-uniform heating. Such improvements are essential to enhance predictive accuracy in complex thermal environments.

4.2.2. Toshiba 37-pin configuration

The validation of the Toshiba 37-pin configuration involved temperature verification at multiple subchannels (CH1, CH4, CH8, CH17, CH26, CH42, CH43, CH56, and CH65) using outlet data from both experiments and CFD simulations. Test scenarios, detailed in Table 4, varied inlet temperatures, flow rates, power levels, and heating patterns to evaluate the thermal response and accuracy of the computational model. Fig. 17 compares experimental and CFD results across these tests, illustrating the model's accuracy under different conditions, while Fig. 18 presents the temperature contours at the bundle outlet, showcasing the influence of heating patterns on thermal distribution.

In Tests E37P02, C37P06, and E37P13, all fuel pins were uniformly heated across three designated regions (Regions I, II, and III). The CFD and experimental results exhibited strong agreement, with a maximum error of 12 % observed at edge subchannel CH56 during Test E37P02. These results confirmed the model's capability to predict uniform heat transfer trends accurately across a larger bundle. In Tests E37P17, E37P20, and F37P27, varying heat generation gradients were applied among the three regions, introducing moderate thermal non-uniformities. The maximum error was 9.6 %, observed at subchannel CH65 during Test E37P17. Despite these variations, the CFD model captured the general trends in temperature distributions with

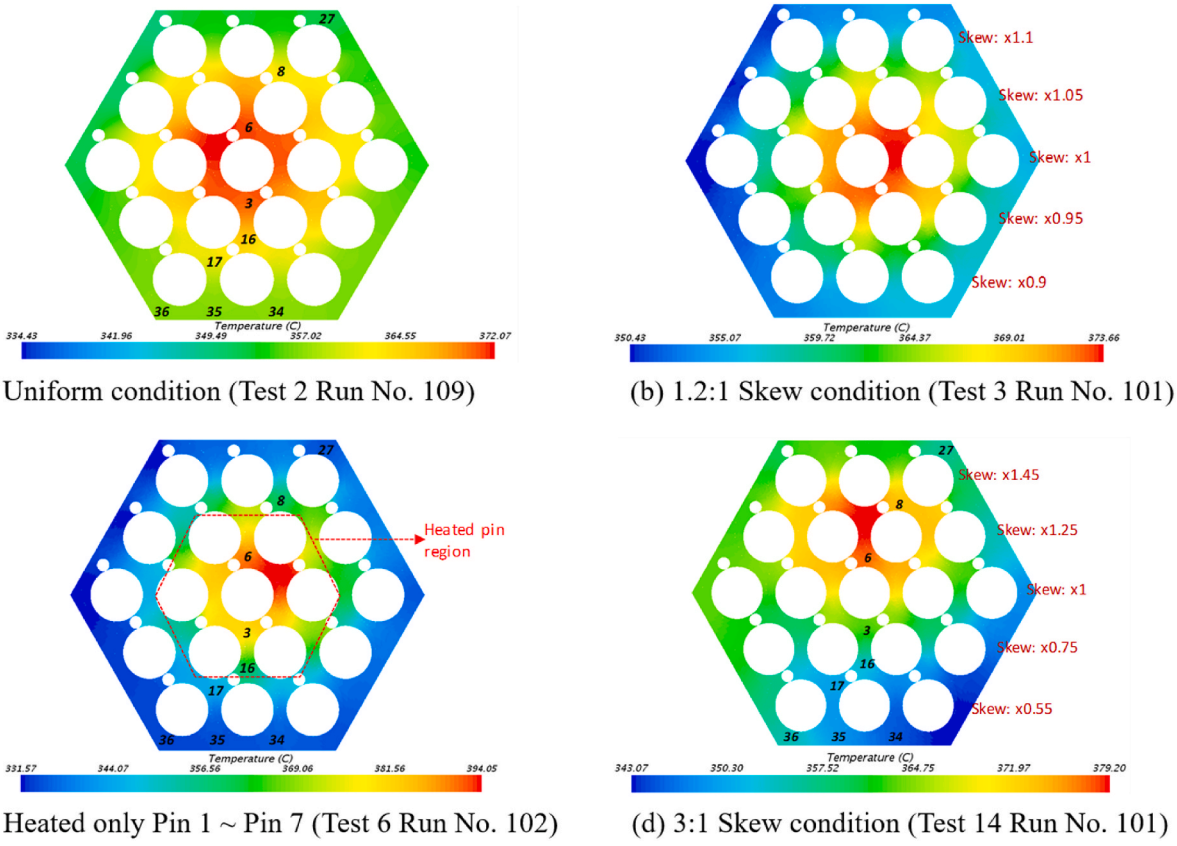

Fig. 16. Temperature contour at bundle outlet of ORNL 19-pin fuel bundle.

reasonable accuracy, demonstrating its robustness in handling moderate heat gradients.

In Tests G37P22, G37P25, and L37P43, extreme heat skew conditions were applied across the three regions. These scenarios resulted in significant thermal gradients and increased uncertainty in turbulent heat transfer predictions. The maximum error reached 18.2 % at subchannel CH65 during Test G37P22, with notable discrepancies in edge subchannels CH56 and CH65. These errors highlight the challenges of modeling complex interactions between turbulence and heat transfer under conditions of extreme heat flux gradients. These findings emphasize the importance of incorporating advanced turbulence models and refining boundary condition specifications to improve predictive accuracy. Such enhancements are crucial for scenarios involving non-uniform heating, especially in larger fuel bundles where the complexity of thermal and flow behaviors increases.

4.2.3. WARD 61-pin configuration

The validation of the WARD 61-pin configuration involved temperature verification at multiple subchannels (CH1, CH4, CH8, CH17, CH26, CH42, CH43, CH56, and CH65) using temperature data collected at the top, middle, and bottom of the heated section during experiments. Test scenarios, detailed in Table 4, included varying pin skew ratios and flow conditions to evaluate the thermal response and the computational model's accuracy. Fig. 19 compares experimental and CFD results for these tests, illustrating the model's ability to capture complex thermal behaviors, while Fig. 20 presents the temperature contours at different sections of the bundle, emphasizing the effects of heating patterns on thermal distribution. In **Test 226**, where uniform heating was applied across all pins, the results displayed consistent temperature distributions, with a **maximum error of 10.1 % observed at subchannel CH47**. This scenario demonstrated the model's ability to accurately predict heat transfer trends under uniform heating conditions in a larger bundle, aligning with the trends observed in Sections 4.2.1 and 4.2.2.

In **Test 223**, a significant heat skew of **2.8:1** was applied, leading to substantial temperature variations among subchannels. At **Level A**, the temperature difference between CH47 and CH103 reached **88°C**, while at **Level F**, it reduced to **54°C**. The **maximum error observed in CFD predictions was approximately 20.5 %**, primarily due to variations in turbulent heat transfer caused by localized heating. These discrepancies underscore the challenges of accurately modeling extreme thermal gradients, as seen in previous non-uniform heating cases. In **Test 403**, characterized by a **moderate heat skew of 2:0.1**, significant temperature differences persisted between edge and interior subchannels. The **temperature difference between CH47 and CH103 reached approximately 76°C at Level A**. The **CFD results captured the overall temperature trend**, but discrepancies were noted in edge subchannels, where the **maximum error was around 18.7 %**. The primary sources of these errors were **localized turbulence effects** and **geometric uncertainties in experimental setups**, similar to the error trends in other non-uniform heating cases.

These findings highlight the critical need for advanced turbulence models to improve the accuracy of CFD predictions under complex heat flux conditions. Refining boundary condition specifications and incorporating detailed geometry models can further enhance predictive performance, particularly for larger bundles with high thermal and flow complexity. Such improvements are essential for optimizing heat transfer and ensuring the safety and efficiency of sodium-cooled fast reactors.

5. Conclusion

In this study, the thermal and flow characteristics of wire-wrapped fuel bundles in sodium-cooled fast reactors (SFRs) were comprehensively evaluated using high-fidelity CFD simulations (STAR-CCM+ and

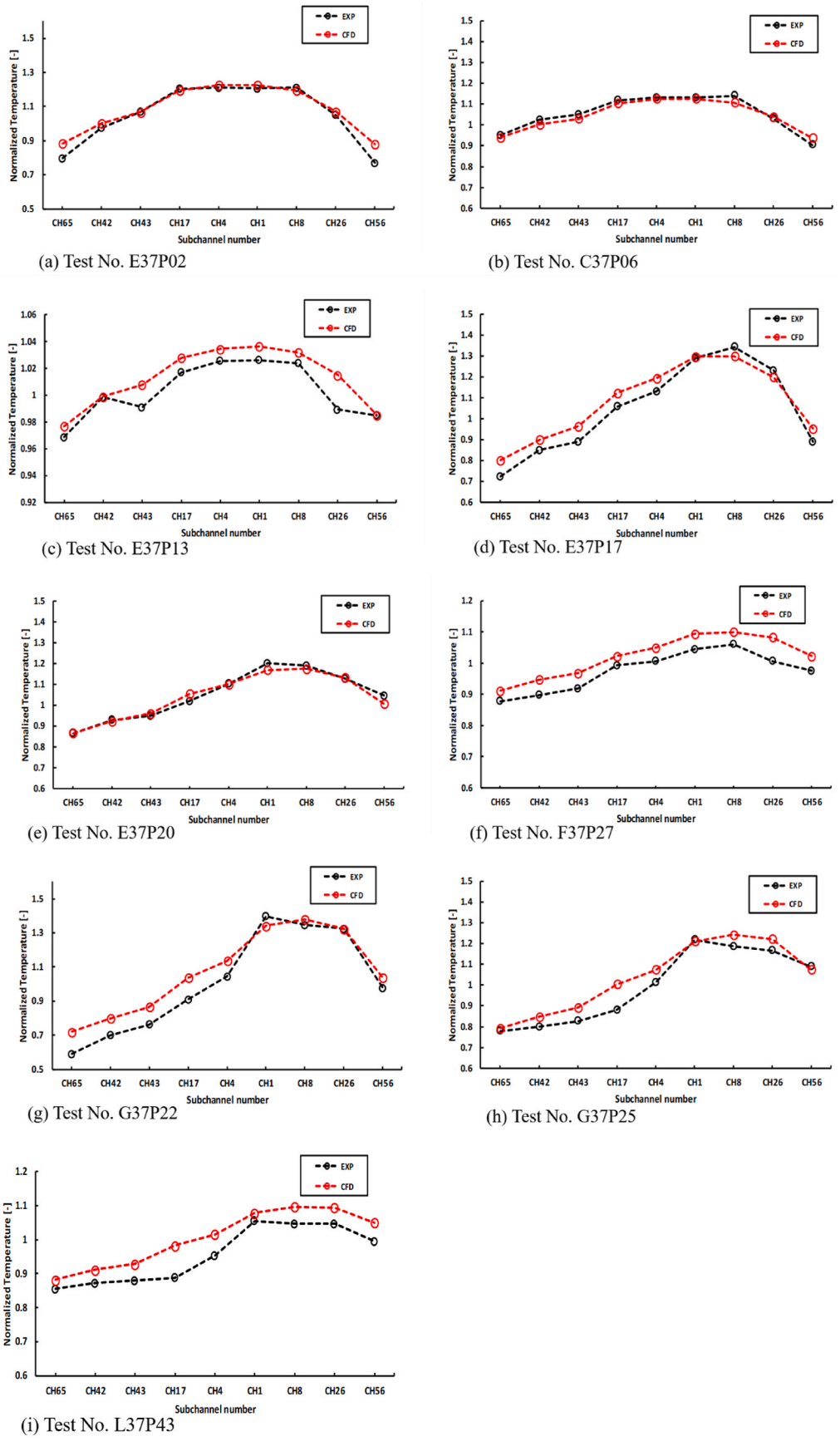

Fig. 17. Comparison of experimental results with CFD results for Toshiba 37-Pin fuel Bundle.

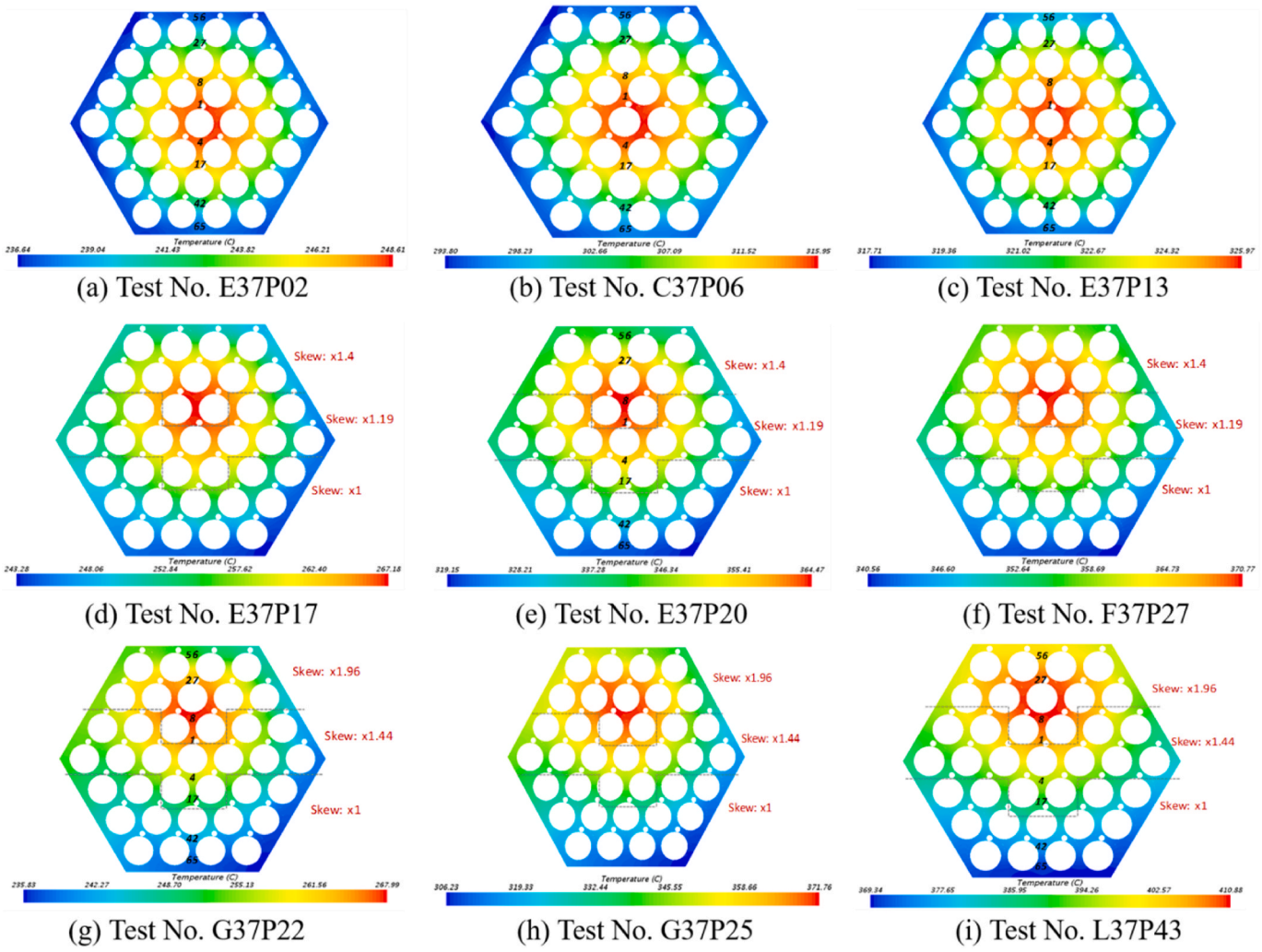

Fig. 18. Temperature contour at bundle outlet of Toshiba 37- Pin fuel Bundle.

ANSYS CFX). It examined various configurations, including the ORNL 19-pin, Toshiba 37-pin, WARD 61-pin, and KAERI 61-pin assemblies, with results validated against experimental data. This systematic approach yielded valuable insights into the influences of geometry, heating patterns, and turbulence modeling on flow and heat transfer behaviors.

The key findings revealed that the SST turbulence model was the most reliable for predicting flow and thermal behaviors across different configurations, effectively balancing the strengths of the k*k*-ε and k*k*-ω models to resolve near-wall turbulence and bulk flow phenomena accurately. Uniform heating scenarios produced consistent errors of approximately 10 %, indicating the robustness of the computational model under standard operating conditions. In contrast, non-uniform heating conditions presented greater challenges, resulting in errors of around 20 %, particularly in edge and corner subchannels. These discrepancies were linked to complex turbulent interactions, localized thermal gradients, and the limitations of current turbulence models in extreme heat flux scenarios.

The significance of these findings lies in their potential to optimize SFR designs by enhancing the understanding of the unique thermal-hydraulic challenges posed by wire-wrapped fuel bundles. Accurately predicting heat transfer and flow characteristics is crucial for ensuring reactor safety, preventing localized overheating, and improving heat removal efficiency. The insights gained also highlight the value of advanced CFD techniques as essential tools in nuclear reactor development.

Challenges identified in the study include the need for more sophisticated turbulence models to address non-uniform heating errors, the impact of geometric sensitivity in experimental setups, and enhancements in turbulent heat transfer modeling for low-prandtl-number fluids like sodium under high thermal gradients.

Future research should focus on developing adaptive and hybrid turbulence models that integrate experimental data to better capture localized heating effects and extreme flow conditions. Targeted sensitivity studies on experimental and computational uncertainties, including mesh refinement and boundary conditions, are also recommended. Additionally, expanding CFD validation to encompass a broader range of operating conditions, such as transient scenarios and higher Reynolds number flows, will enhance model applicability to diverse reactor designs.

By addressing these challenges and building on the findings presented, this research lays a foundation for more reliable and accurate CFD methodologies. These advancements will significantly contribute to the safer and more efficient design of sodium-cooled fast reactors, reinforcing their potential as a sustainable and reliable energy source for the future.

CRediT authorship contribution statement

Jophous Mugabi: Project administration, Data curation, Supervision, Validation, Visualization, Writing – review & editing. **Hanseop Song:** Formal analysis, Investigation, Methodology, Validation,

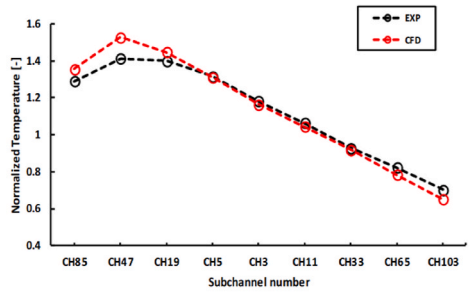

(a) Top of heated section (Level A) of Test No. 223

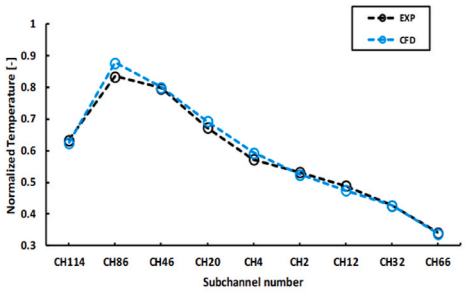

(b) Middle of heated section (Level F) of Test No. 223

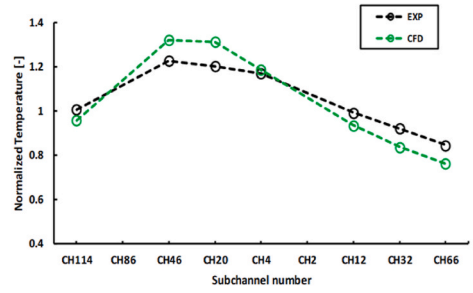

(c) Outlet of the bundle (Level E) of Test No. 223

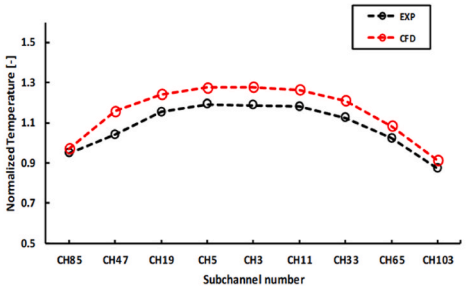

(d) Top of heated section (Level A) of Test No. 226

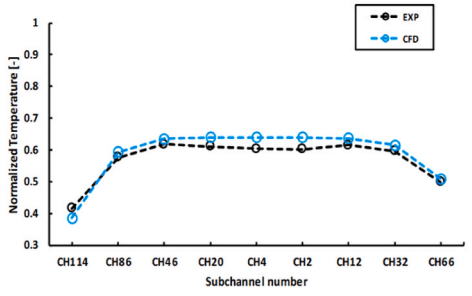

(e) Middle of heated section (Level F) of Test No. 226

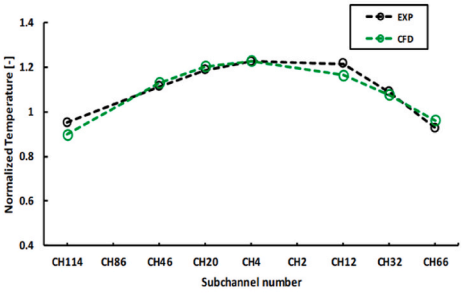

(f) Outlet of the bundle (Level E) of Test No. 226

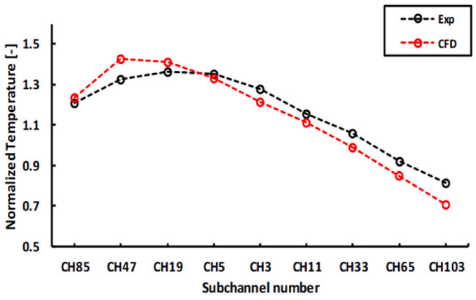

(g) Top of heated section (Level A) of Test No. 403

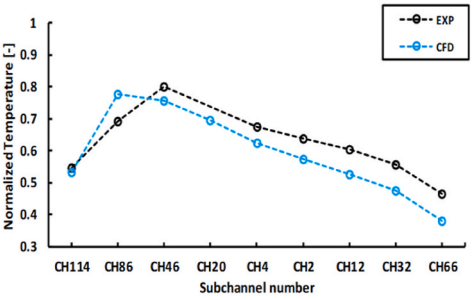

(h) Middle of heated section (Level F) of Test No. 403

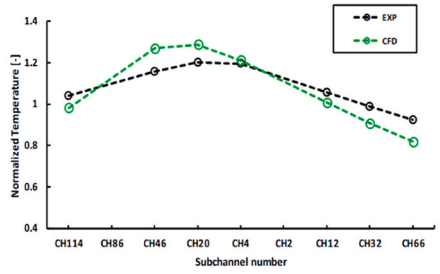

(i) Outlet of the bundle (Level E) of Test No. 403

Fig. 19. Comparison of experimental results with CFD results for WARD 61-pin.

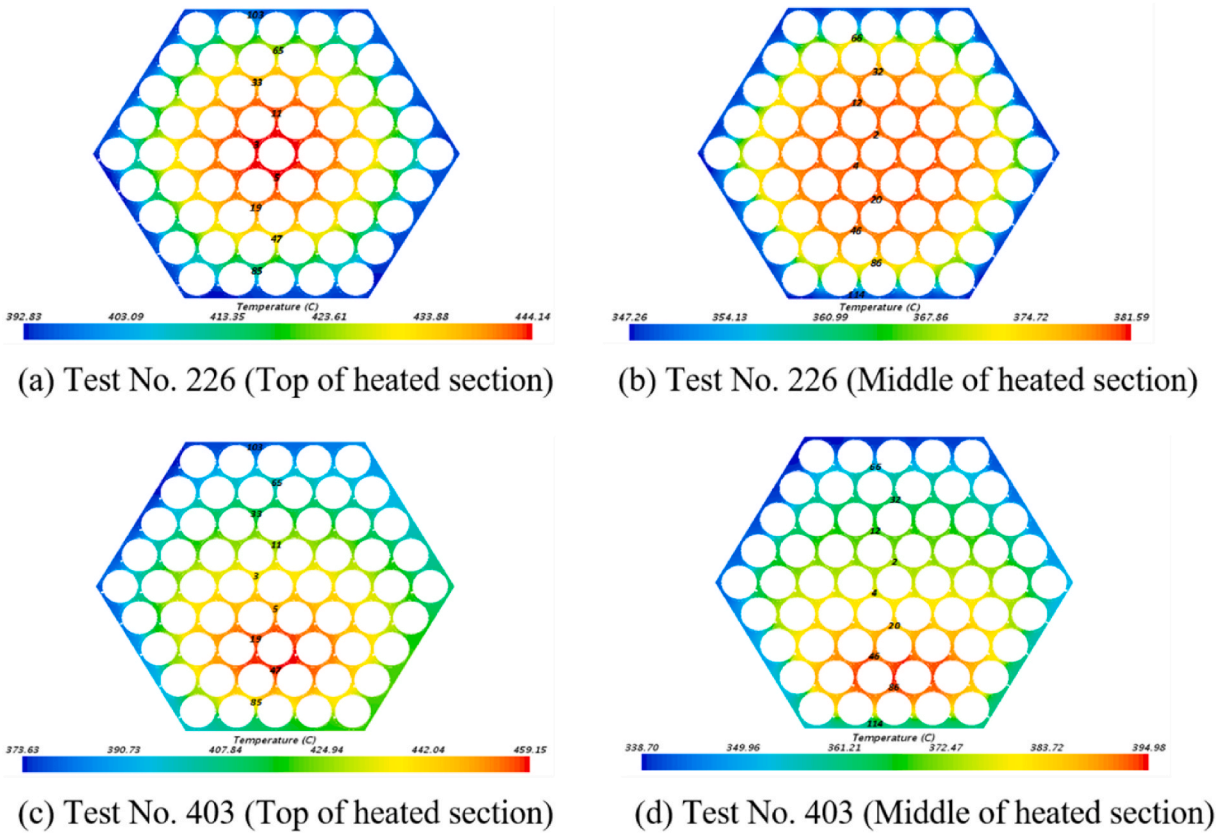

Fig. 20. Temperature contour at bundle outlet and middle of WARD 61-pin.

Visualization, Writing – original draft. **Jae-Ho Jeong:** Conceptualization, Funding acquisition, Methodology, Project administration, Resources; Software, Supervision, Validation, Visualization, Writing – review & editing.

Declaration of competing interest

The authors declare that they have no known competing financial interests or personal relationships that could have appeared to influence the work reported in this paper.

Acknowledgment

This work was supported by the Korea Institute of Energy Technology Evaluation and Planning (KETEP) grant funded by the Korean government (Ministry of Trade, Industry and Energy, MOTIE) under the following projects: RS-2023-00243201 (Global Talent Development Project for Advanced SMR Core Computational Analysis Technology Development) and RS-2024-00487321.

References

[1] W.-S. Kim, Y.-G. Kim, Y.-J. Kim, A subchannel analysis code MATRA-LMR for wire wrapped LMR subassembly, Ann. Nucl. Energy 29 (2002) 303–321, https://doi.org/10.1016/S0306-4549(01)00041-X.
[2] M. Memmott, J. Buongiorno, P. Hejzlar, On the use of RELAP5-3D as a subchannel analysis code, Nucl. Eng. Des. 240 (2010) 807–815, https://doi.org/10.1016/j.nucengdes.2009.11.006.
[3] R.L. Sun, D.L. Zhang, Y. Liang, M.J. Wang, W.X. Tian, S.Z. Qiu, G.H. Su, Development of a subchannel analysis code for SFR wire-wrapped fuel assemblies, Prog. Nucl. Energy 104 (2018) 327–341, https://doi.org/10.1016/j.pnucene.2017.12.005.
[4] J.W. Fricano, E. Baglietto, A quantitative CFD benchmark for Sodium Fast Reactor fuel assembly modeling, Ann. Nucl. Energy 64 (2014) 32–42, https://doi.org/10.1016/J.ANUCENE.2013.09.019.
[5] J.-H. Jeong, M.-S. Song, CFD investigation of a JAEA 7-pin fuel assembly experiment with local blockage for SFR, Nucl. Eng. Technol. 53 (2021) 3207–3216, https://doi.org/10.1016/j.net.2021.05.009.
[6] S. He, M. Wang, Y. Hou, W. Tian, S. Qiu, G.H. Su, Study on the flow and heat transfer characteristics of liquid sodium in a hexagonal 7-rod bundle, Nucl. Eng. Des. 393 (2022) 111798, https://doi.org/10.1016/j.nucengdes.2022.111798.
[7] M.S. Song, J.H. Jeong, E.S. Kim, Numerical investigation on vortex behavior in wire-wrapped fuel assembly for a sodium fast reactor, Nucl. Eng. Technol. 51 (2019) 665–675, https://doi.org/10.1016/J.NET.2018.12.012.
[8] M. Wang, H. Ju, J. Wu, H. Qiu, K. Liu, W. Tian, G.H. Su, A review of CFD studies on thermal hydraulic analysis of coolant flow through fuel rod bundles in nuclear reactor, Prog. Nucl. Energy 171 (2024) 105175, https://doi.org/10.1016/j.pnucene.2024.105175.
[9] A. Shams, A. De Santis, L.K. Koloszar, A. Villa Ortiz, C. Narayanan, Status and perspectives of turbulent heat transfer modelling in low-Prandtl number fluids, Nucl. Eng. Des. 353 (2019) 110220, https://doi.org/10.1016/j.nucengdes.2019.110220.
[10] L. Bricteux, M. Duponcheel, G. Winckelmans, I. Tiselj, Y. Bartosiewicz, Direct and large eddy simulation of turbulent heat transfer at very low Prandtl number: application to lead–bismuth flows, Nucl. Eng. Des. 246 (2012) 91–97, https://doi.org/10.1016/j.nucengdes.2011.07.010.
[11] H. Kawamura, H. Abe, Y. Matsuo, DNS of turbulent heat transfer in channel flow with respect to Reynolds and Prandtl number effects, Int. J. Heat Fluid Flow 20 (1999) 196–207, https://doi.org/10.1016/S0142-727X(99)00014-4.
[12] L. Liu, U. Ahmed, N. Chakraborty, A comprehensive evaluation of turbulence models for predicting heat transfer in turbulent channel flow across various Prandtl number regimes, Fluids 9 (2024) 42, https://doi.org/10.3390/FLUIDS9020042, 2024, Vol. 9, Page 42.
[13] Z. Xue, Y. Hongxing, D. Jian, D. Sijia, W. Xiaoyu, F. Wenpei, Study on the turbulent Prandtl number model for liquid metal flow and heat transfer in a narrow rectangular channel, Front. Energy Res. 12 (2024) 1366470, https://doi.org/10.3389/fenrg.2024.1366470.
[14] G. Choi, S. Yoon, M. Song, J.H. Jeong, High-fidelity numerical investigation on elucidating sodium heat transfer characteristics for 37-pin wire-wrapped fuel bundle in the PLANDTL facility, Int. J. Energy Res. 2023 (2023), https://doi.org/10.1155/2023/8834634.
[15] M.H. Fontana, R.E. MacPherson, P.A. Gnadt, L.F. Parsly, J.L. Wantland, Temperature distribution in the duct wall and at the exit of a 19-rod simulated LMFBR fuel assembly (FFM bundle 2A), Nucl. Technol. 24 (1974) 176–200, https://doi.org/10.13182/NT74-A31474.
[16] F. Namekawa, A. Ito, K. Mawatari, Buoyancy effects on wire-wrapped rod bundle heat transfer in an LMFBR fuel assembly, AICHE Symp. Ser. 80 (1984) 128–133.

http://pascal-francis.inist.fr/vibad/index.php?action=getRecordDetail&idt=8983799. (Accessed 11 November 2024).
[17] F.C. Engel, B. Minushkin, R.J. Atkins, R.A. Markley, Characterization of heat transfer and temperature distributions in an electrically heated model of an LMFBR blanket assembly, Nucl. Eng. Des. 62 (1980) 335–347, https://doi.org/10.1016/0029-5493(80)90037-0.
[18] J.-H. Jeong, M.-S. Song, K.-L. Lee, RANS based CFD methodology for a real scale 217-pin wire-wrapped fuel assembly of KAERI PGSFR, Nucl. Eng. Des. 313 (2017) 470–485, https://doi.org/10.1016/j.nucengdes.2017.01.007.
[19] M. Song, J.-H. Jeong, E.S. Kim, Investigation on subchannel flow distribution in wire-wrapped 37 and 61-pin bundle using computational fluid dynamics, Nucl. Eng. Des. 370 (2020) 110904, https://doi.org/10.1016/j.nucengdes.2020.110904.
[20] H. Kawamura, K. Ohsaka, H. Abe, K. Yamamoto, DNS of turbulent heat transfer in channel flow with low to medium-high Prandtl number fluid, Int. J. Heat Fluid Flow 19 (1998) 482–491, https://doi.org/10.1016/S0142-727X(98)10026-7.
[21] J. Smagorinsky, General circulation experiments with the primitive equations, Mon. Weather Rev. 91 (1963) 99–164, https://doi.org/10.1175/1520-0493(1963)091<0099:GCEWTP>2.3.CO;2.
[22] D.C. Wilcox, Formulation of the k-w turbulence model revisited, AIAA J. 46 (2008) 2823–2838, https://doi.org/10.2514/1.36541.
[23] D.C. Wilcox, Reassessment of the scale-determining equation for advanced turbulence models, AIAA J. 26 (1988) 1299–1310, https://doi.org/10.2514/3.10041.
[24] F.R. Menter, Improved Two-Equation K-Omega Turbulence Models for Aerodynamic Flows, Moffett Field, CA, United States, 1992. https://ntrs.nasa.gov/citations/19930013620. (Accessed 11 November 2024).
[25] F.R. Menter, Zonal two equation k-ω turbulence models for aerodynamic flows, in: Fluid Dynamics, American Institute of Aeronautics and Astronautics, Inc. AIAA-93-2906, Reston, 1993, pp. 1–22. https://cfd.spbstu.ru/agarbaruk/doc/1993_Menter_ZonalTwoEquationk-wTurbulenceModelsforAerodynamicFlows(2).pdf.
[26] Siemens, Simcenter STAR-CCM+2210 user guide 17.06.007. https://blogs.sw.siemens.com/simcenter/simcenter-star-ccm-2210-released-whats-new/, 2022. (Accessed 11 November 2024).
[27] K. Rehme, Pressure drop correlations for fuel element spacers, Nucl. Technol. 17 (1973) 15–23, https://doi.org/10.13182/NT73-A31250.
[28] S.K. Chen, Y.M. Chen, N.E. Todreas, The upgraded Cheng and Todreas correlation for pressure drop in hexagonal wire-wrapped rod bundles, Nucl. Eng. Des. 335 (2018) 356–373, https://doi.org/10.1016/j.nucengdes.2018.05.010.
[29] S.-K. Cheng, N.E. Todreas, Hydrodynamic models and correlations for bare and wire-wrapped hexagonal rod bundles — bundle friction factors, subchannel friction factors and mixing parameters, Nucl. Eng. Des. 92 (1986) 227–251, https://doi.org/10.1016/0029-5493(86)90249-9.
[30] F.C. Engel, R.A. Markley, A.A. Bishop, Laminar, transition, and turbulent parallel flow pressure drop across wire-wrap-spaced rod bundles, Nucl. Sci. Eng. 69 (1979) 290–296, https://doi.org/10.13182/NSE79-A20618.
[31] S.R. Choi, H. Kim, S.-K. Chang, H.S. Choi, D.-J. Euh, H.-Y. Lee, W.S. Yang, Assessment of subchannel flow mixing coefficients for wire-wrapped hexagonal fuel rod bundles, Ann. Nucl. Energy 166 (2022) 108810, https://doi.org/10.1016/j.anucene.2021.108810.
[32] S.-K. Chang, D.-J. Euh, S. Kim, H.S. Choi, H. Kim, Y.J. Ko, S.R. Choi, H.-Y. Lee, Experimental study of the flow characteristics in an SFR type 61-pin rod bundle using iso-kinetic sampling method, Ann. Nucl. Energy 106 (2017) 160–169, https://doi.org/10.1016/j.anucene.2017.03.024.
[33] K. Sawada, A convenient visualization method for identifying vortex centers, Trans. Jpn. Soc. Aeronaut. Space Sci. 38 (1995) 102–116. https://cir.nii.ac.jp/crid/1571980073987089536?lang=en. (Accessed 11 November 2024).